Lithospheric structure of Tasmania from a novel form of teleseismic tomography

N. Rawlinson,[1] A. M. Reading,[1] and B. L. N. Kennett[1]

Received 28 April 2005; revised 6 September 2005; accepted 14 September 2005; published 3 February 2006.

[1] In 2001 and 2002, a temporary array of 72 seismic recorders was deployed across northern Tasmania (SE Australia), with the aim of imaging the underlying crust and upper mantle using three-dimensional (3-D) teleseismic tomography. Using a recently developed adaptive stacking technique, 6520 relative *P* wave arrival time residuals have been picked from 101 distant earthquake records spanning a 5 month period. A novel iterative nonlinear tomographic procedure based on a subspace inversion scheme and the fast marching method, a grid-based eikonal solver, is used to map the residual patterns as *P* wave velocity anomalies. The new scheme proves to be both fast and robust, making it well suited to large data sets and the reconstruction of complex anomalies. The resultant tomographic images of Tasmania exhibit significant lateral perturbations in *P* wave velocity structure ($\leq$5%) from a 1-D reference model. A marked transition from higher velocities in the east to lower velocities in the west strongly supports the idea that eastern Tasmania is underlain by dense rocks with an oceanic crustal affinity, contrasting with the continentally derived siliciclastic core of western Tasmania. Significantly, the Tamar Fracture System does not overlie the narrow transition from relatively fast to slow velocities, which suggests that it may be a near-surface feature rather than a manifestation of deeper crustal-scale suturing as previously thought. Farther west, an easterly dipping zone of relatively high velocity material beneath the Rocky Cape Group and Arthur Lineament may be related to remnant subduction of oceanic lithosphere associated with the mid-Cambrian Delamerian Orogeny.

Citation: Rawlinson, N., A. M. Reading, and B. L. N. Kennett (2006), Lithospheric structure of Tasmania from a novel form of teleseismic tomography, *J. Geophys. Res.*, *111*, B02301, doi:10.1029/2005JB003803.

1. Introduction

[2] Prior to the early 1990s, few studies attempted to image the three-dimensional (3-D) seismic structure of the Australian lithosphere in part or whole. This changed with the continent-wide SKIPPY project (1993–1998), which involved the successive deployment of portable arrays of broadband seismometers to record regional earthquakes, principally from the margins of the Australian plate. In total, 65 sites were occupied with a nominal station spacing of approximately 400 km. Surface wave data from SKIPPY and subsequent deployments have been used to construct 3-D tomographic images of shear wave speed variations in the Australian lithosphere and underlying mantle to a maximum horizontal resolution of approximately 200–250 km [*Zielhuis and van der Hilst*, 1996; *Debayle and Kennett*, 2000; *Simons et al.*, 2002; *Debayle and Kennett*, 2003; *Fishwick et al.*, 2005]. Major features of these images include: a marked transition from slow shear velocities beneath Phanerozoic eastern Australia to fast shear velocities beneath Precambrian western Australia; a pattern of pronounced low velocities along the eastern seaboard which correlate well with the presence of recent volcanism; a high velocity anomaly beneath western Australia which extends to over 250 km depth beneath Archean and Proterozoic Cratons. These results have had a major impact on the understanding of the structure and evolution of the Australian continent.

[3] Following on from the SKIPPY project, the emphasis of passive tomographic imaging studies has been on higher density, more localized seismic arrays placed in regions of particular geological interest. For example, the MALT project involved three separate deployments of 40 short-period seismometers with a nominal station spacing of 50 km across south east Australia over the period 1998–2000. To date, only data from the southernmost array (LF98) has been used to image the 3-D *P* wave speed structure of the crust and upper mantle using teleseismic travel time tomography [*Graeber et al.*, 2002]. However, these initial results reveal a number of significant features, including pronounced negative velocity anomalies in the vicinity of the recent Newer Volcanic Province in western Victoria, and that the Moyston Fault Zone appears to represent a lithospheric-scale suture zone between the early Paleozoic Delamerian Orogen and the Lachlan Orogen (see Figure 1).

[4] TIGGER, a multifaceted seismic study of Tasmania and southern Victoria, was undertaken by the Research

[1]Research School of Earth Sciences, Australian National University, Canberra, Australia.

0148-0227/06/2005JB003803$09.00

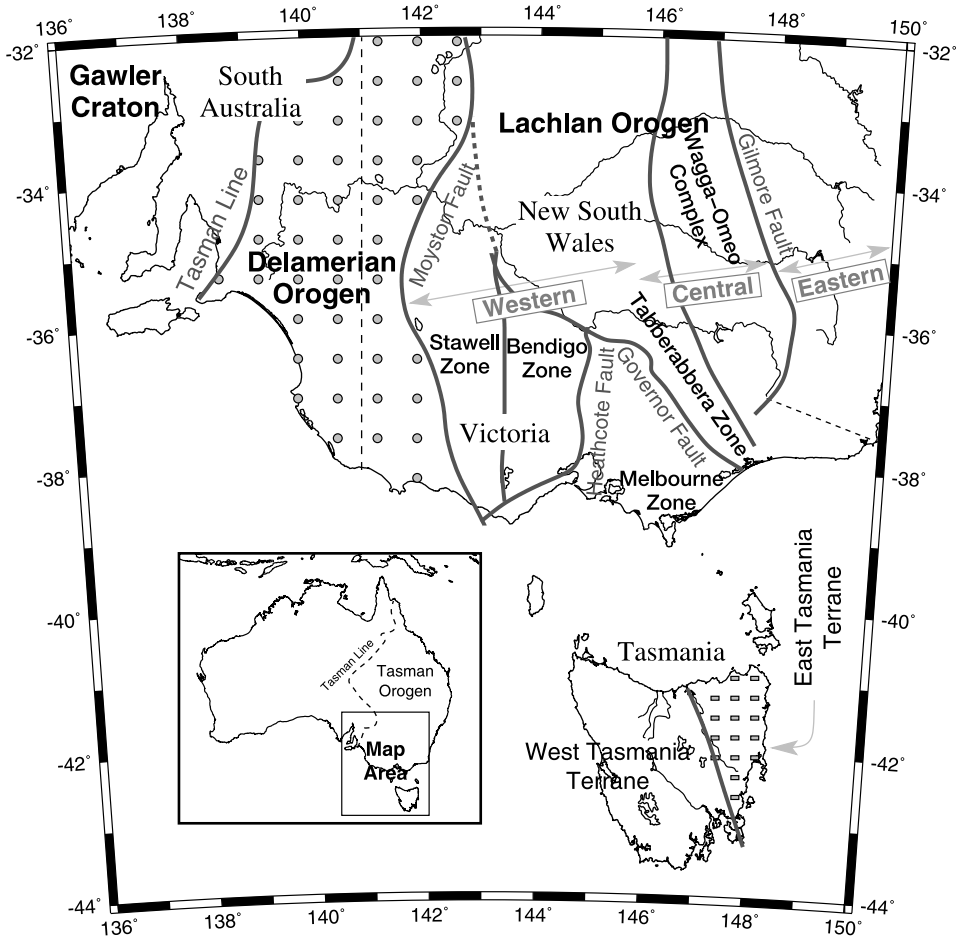

Figure 1. Schematic map of the southern Tasman Orogen in eastern Australia (based on maps of *Foster and Gray* [2000], *Cayley et al.* [2002], and *Willman et al.* [2002]). The Phanerozoic terranes of the Lachlan and Delamerian orogens in the east are juxtaposed against the older Precambrian rocks of western Australia along the Tasman Line.

School of Earth Sciences at the Australian National University in 2001–2002. One component of TIGGER involved the deployment of 72 short-period and broadband seismometers across northern Tasmania for a period of 5 months to record distant earthquakes suitable for use in teleseismic tomography. With a nominal station spacing of 15 km and a good azimuthal coverage of teleseisms, the high-density seismic array permits detailed imaging of the crust and lithospheric mantle.

[5] There are a number of issues regarding the structure, composition and tectonic history of the lithosphere in this region of Australia that are the subject of current debate. First, the geological relationship between Tasmania and mainland Australia appears ambiguous [*Elliot et al.*, 1991; *Cayley et al.*, 2002]. In particular, the lack of Precambrian outcrop within the Lachlan Orogen is in marked contrast to the prolific exposure of Proterozoic rocks in western Tasmania. Second, the so-called Tamar Fracture System (TFS), previously regarded as the surface expression of crustal-scale suturing, may be a thin skinned feature [*Leaman*, 1994; *Reed et al.*, 2002] unrelated to the formation of a major lithospheric boundary. Finally, there are several competing plate tectonic models for the early mid-Phanerozoic evolution of Tasmania [*Corbett et al.*, 1972; *Crawford and Berry*, 1992; *Reed et al.*, 2002], which involve various combinations of subduction, obduction, deposition, extension and volcanism. The detailed 3-D seismic images of the lithosphere beneath northern Tasmania presented in this paper have the potential to make valuable contributions toward resolving each of these issues.

[6] The teleseismic tomography principle that we employ to permit 3-D imaging of the lithosphere beneath the TIGGER array from distant earthquakes has had a long and venerable history [*Aki et al.*, 1977; *Oncescu et al.*, 1984; *Humphreys and Clayton*, 1990; *Benz et al.*, 1992; *Achauer*, 1994; *Saltzer and Humphreys*, 1997; *Steck et al.*, 1998; *Graeber et al.*, 2002]. The key assumption is that relative arrival time residuals across the receiver array are largely unaffected by lateral variations in structure outside a local model volume defined beneath the array. Two 3-D teleseismic tomography schemes that are currently in common usage are those of *VanDecar* [1991] and *Steck et al.* [1998], both of which use ray tracing to solve the forward problem of predicting travel time residuals for a given model.

[7] To take advantage of recent developments in grid-based wave front tracking, we introduce a new iterative nonlinear teleseismic tomography scheme to interpret the

TIGGER array data. The new scheme uses uniform cubic B spline functions to define a continuous smooth velocity field from a 3-D grid of velocity nodes in spherical coordinates. In order to calculate the travel time field throughout the model volume, the Fast Marching Method or FMM [*Sethian*, 1996; *Sethian and Popovici*, 1999] is used. FMM is a grid-based eikonal solver which combines computational efficiency and unconditional stability, making it ideally suited to tomographic imaging problems. A subspace inversion scheme [*Kennett et al.*, 1988] is used to solve the inverse problem of adjusting the values of the velocity nodes in order to satisfy the observed data and regularization constraints. The characteristics and benefits of the new tomographic scheme are demonstrated by its application to the TIGGER data set, and the robustness of the imaging results is analyzed using resolution tests with synthetic data.

2. Geological Setting

[8] By the end of the Proterozoic, the Australian continent comprised an assemblage of the north, west and south Australian cratons. The onset of the Phanerozoic ushered in a new phase in the evolution of the Australian continent, with predominantly subduction related accretion adding nearly one third of the present-day continental lithosphere to the eastern margin of Precambrian Australia [*Betts et al.*, 2002]. This younger region of the lithosphere is often referred to as the Tasman Orogen or "Tasmanides" [e.g., *Foster and Gray*, 2000], and comprises the Delamerian, Lachlan and New England orogens.

[9] In south east Australia, the Delamerian Orogeny (Figure 1) began in the Middle Cambrian, with convergence along the proto-Pacific margin [*Betts et al.*, 2002] culminating in west vergent foreland style folds and high-temperature, low-pressure metamorphism associated with intrusive magmatism. The transition from Precambrian western Australia to Phanerozoic eastern Australia is often represented by a largely inferred "Tasman Line" (Figure 1), which may either represent an orogenic suture or basin boundary, the latter possibly caused by the breakup of Rodinia. However, recent potential field data [*Direen and Crawford*, 2003] suggests that the transition is too complex to be represented by a simple line. *Kennett et al.* [2004] discuss the relationship between seismic observations and various interpretations of the Tasman Line.

[10] The evolution of the Lachlan Orogen (Figure 1), which began in the Late Cambrian and was largely complete by the Middle to Late Devonian, is highly complex, and may involve multiple subduction complexes. *Foster and Gray* [2000] favor a tectonic model involving the interaction of oceanic microplates, a volcanic island arc and multiple turbidite-dominated thrust systems; a total of three subduction zones, one in each of the western, central and eastern subprovinces, are invoked. *Fergusson* [2003] uses a similar model to explain the evolution of the Lachlan Orogen, but requires an additional subduction zone along the eastern margin of the Melbourne Zone.

[11] However, the proposed subduction-accretion model for the central and western subprovinces is not universally accepted. For example, *Taylor and Cayley* [2000] argue that the structural style and intermediate grade metamorphism is consistent with the simpler interpretation of an intraplate collapse of a marginal sea driven by outboard convergence. On the basis of argon ages derived from micas in western and central Victoria, *VandenBerg* [1999] argues that the pattern of deformation over time within the Lachlan Orogen is not consistent with the progressive subduction of crustal material. This lack of consensus can be attributed to the complexity of the surface geology, the presence of overlying Mesozoic and Cenozoic basins obscuring large regions of Paleozoic terrane, the difficulty of recognizing ancient subduction systems, and a limited knowledge of the deep structure and composition of the lithosphere.

[12] In the Early to Middle Phanerozoic, Tasmania largely comprised what is now referred to as the West Tasmania Terrane (Figure 2). The evolution of this region began as long ago as 800–750 Ma [*Turner et al.*, 1998], with prolific granite emplacement on King Island and deposition of thick turbidite piles in NW Tasmania. The major event which shaped western Tasmania was the Middle to Late Cambrian Tyennan Orogeny, which was a period of substantial deformation, underscored by the presence of significant metamorphism and emplacement of serpentinitic thrust sheets [*Elliot et al.*, 1993]. Early models of the Tyennan Orogeny included a wide range of scenarios, from westerly subduction to easterly subduction to even a purely extensional regime in which the felsic Mount Read Volcanic arc formed as a result of rifting [*Corbett et al.*, 1972]. More recently, the model of *Crawford and Berry* [1992] and *Crawford et al.* [2003] has gained wider acceptance. In this model, plume triggered rifting is followed by east dipping subduction to produce an intraoceanic volcanic arc, which is subsequently obducted westward by arc-continent collision. The thickened crust then collapses because of postcollisional extension which produces the Mount Read Volcanics, and exhumation of underthrust continental crust follows.

[13] The East Tasmania Terrane (Figure 2) contains no evidence of the Tyennan Orogeny or Proterozoic outcrop, and it is widely thought that the two terranes were juxtaposed during the Middle Devonian Tabberabberan Orogeny [*Elliot et al.*, 1993]. A long held view has been that the so-called Tamar Fracture System (Figure 2) marks the zone of a crustal-scale suture between the East and West Tasmania terranes [*Williams*, 1989]. The main basis for this argument is the difference in stratigraphy across the Tamar River in northern Tasmania; Proterozoic sedimentary and Paleozoic volcanic and sedimentary successions lie to the west, while a thick sequence of Lower to Middle Paleozoic turbidites lie to the east [*Reed*, 2001]. However, south of the Tamar Valley, any evidence of a crustal scale suture zone is obscured by late Carboniferous sedimentary deposits and Jurassic dolerite sheets. In addition, potential field data [*Leaman*, 1994] do not support the existence of a major terrane boundary beneath the inferred Tamar Fracture System (Figure 2).

[14] The relationship between Tasmania and the mainland Phanerozoic terranes is another area of controversy. The presence of exposed Precambrian blocks in western Tasmania appears to exclude a tectonic affinity with the Lachlan Orogen [*Elliot et al.*, 1991]; however, the similarity of Devonian granites in southern Victoria and northern Tasmania suggests that Tasmania was in its current position by the Middle Paleozoic [*Reed*, 2001]. Recently, it has been

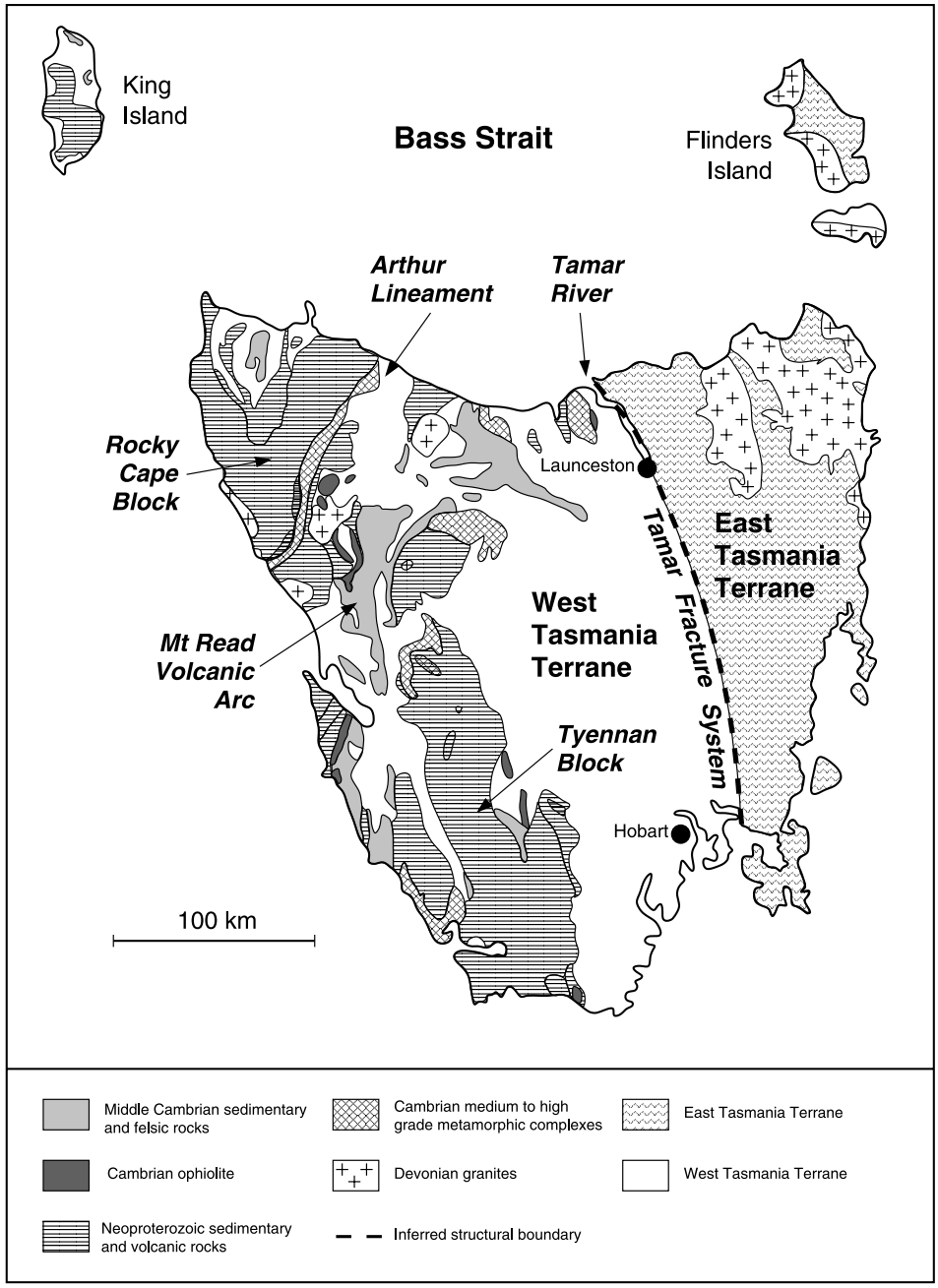

Figure 2. Simplified geological map of Tasmania showing major structural and stratotectonic features (modified from *Spaggiari et al.* [2003] with permission of the Geological Society of Australia). The boundary between the East and West Tasmania terranes is largely obscured by post-Devonian cover sequences (not shown). The so-called Tamar Fracture System has traditionally been extrapolated southward from the Tamar Valley to mark the location of a crustal-scale suture zone.

suggested by *Cayley et al.* [2002], mainly on the basis of potential field data, that the Proterozoic crust of western Tasmania extends northward under Bass Strait and forms the basement beneath the sedimentary cover of the Melbourne Zone (Figure 1). *Direen and Crawford* [2003] use evidence from tholeiites in western New South Wales, western Victoria, eastern South Australia and Tasmania to interpret the presence of a volcanic rift margin at the end of the Neoproterozoic. The presence of younger boninitic rocks indicates that this was followed by a forearc collision with an east dipping subduction zone in the Late Cambrian. This suggests that the evolution of Tasmania and mainland Australia are closely linked, and that the Tyennan Orogeny in Tasmania is in fact the southern extension of the mainland Delamerian Orogeny.

3. The TIGGER Experiment

[15] The TIGGER experiment aims to achieve a better understanding of Tasmania's deep geology, tectonic evolution, and relationship with mainland Australia. The field component of TIGGER began in October 2001 with the

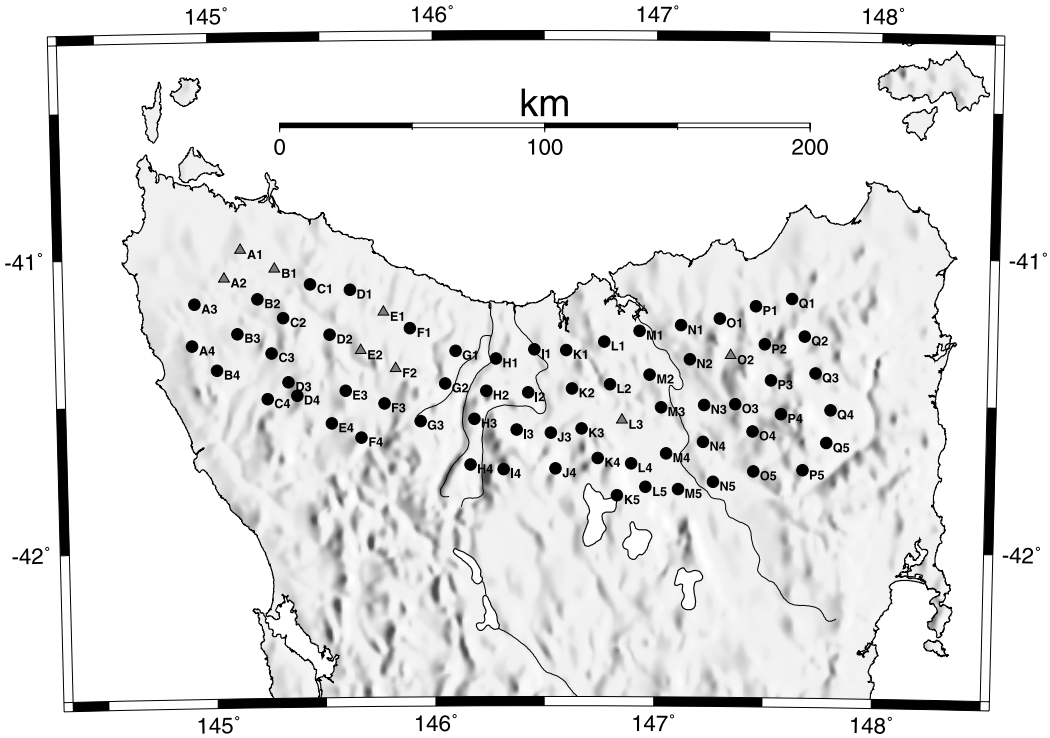

Figure 3. Locations of the 64 short-period (black dots) and eight broadband (grey triangles) stations that make up the TIGGER seismic array in northern Tasmania. Stations vary in elevation between 30 m (I1) and 1105 m (K5).

deployment of 13 three component broadband seismic recorders throughout Tasmania for a 10 month period; this was followed in December by an additional four broadband recorders in southern Victoria for a period of 5 months. The final stage of fieldwork began in March 2002 with a 5 month deployment of 64 vertical component short-period seismometers across northern Tasmania with a nominal station spacing of 15 km. Eight of the broadband recorders from the 2001 deployment lie within the short-period array. The 72 stations of the TIGGER seismic array are shown in Figure 3 and provide all the travel time data that are used in this paper to constrain the 3-D tomographic results. In related work, preliminary results from receiver function analysis using records from the broadband stations can be found in *Reading* [2005], and *Fishwick et al.* [2005] include Rayleigh waveform data from selected broadband stations to help constrain surface wave tomography maps of the Australian continent.

[16] A number of considerations influenced the final location and geometry of the seismic array (Figure 3). First, an east-west traverse across northern Tasmania provides good coverage of the transition between the East and West Tasmania terranes, the Arthur Lineament, and the Mount Read Volcanics. Second, much of southwest Tasmania is inaccessible by road, making a dense deployment of seismometers in this region a logistically complex and expensive task. Finally, a station spacing of approximately 15 km allows the mid-lower crust and lithospheric mantle to be well constrained by teleseismic arrivals, provided they have good azimuthal coverage. Results from geological mapping and potential field data [*Leaman*, 1989; *Elliot et al.*, 1993; *Gunn et al.*, 1997] indicate that, at least near the surface, major geological features have a relatively short wavelength, and that a larger station spacing may result in the omission of important detail.

[17] During the operation of the TIGGER array, 101 teleseismic events with sufficient signal-to-noise ratios to permit the extraction of reliable arrival time residual maps were recorded (see Figure 4). The distribution of these events suggests that path coverage from the north and east of the array will be high, but to the south and west, coverage will be relatively poor. Undoubtedly, this significant variation in the azimuthal distribution of events will effect the recovery of structure. This is examined further in section 6.1 using synthetic resolution tests, which are better able to gauge the resolving power of the data set. Most of the arrivals identified in the records of the 101 teleseismic events are the direct *P* phase; however, a variety of other phases are also picked, including *pP*, *PP*, *PcP*, *ScP*, and *PKiKP*. In total, 110 arrivals from various phases have been identified, resulting in the availability of up to 7920 paths to constrain the tomographic inversion.

[18] Seismic records from four different events recorded by the TIGGER array are shown in Figure 5. All traces are approximately aligned by using predictions from the ak135 global reference model [*Kennett et al.*, 1995] to account for moveout; any remaining misalignment can be attributed to lateral variations in structure beneath the array. Signal-to-noise ratios of traces from the Mariana Islands (Figure 5a) and Fiji Islands (Figure 5c) events are generally high, and have relatively clear onsets. However, records from the South Sandwich Islands event (Figure 5b) have a lower signal-to-noise ratio and most onsets of *P* are difficult to identify. The *PcP* phase from the Vanuatu Islands (Figure 5d) is

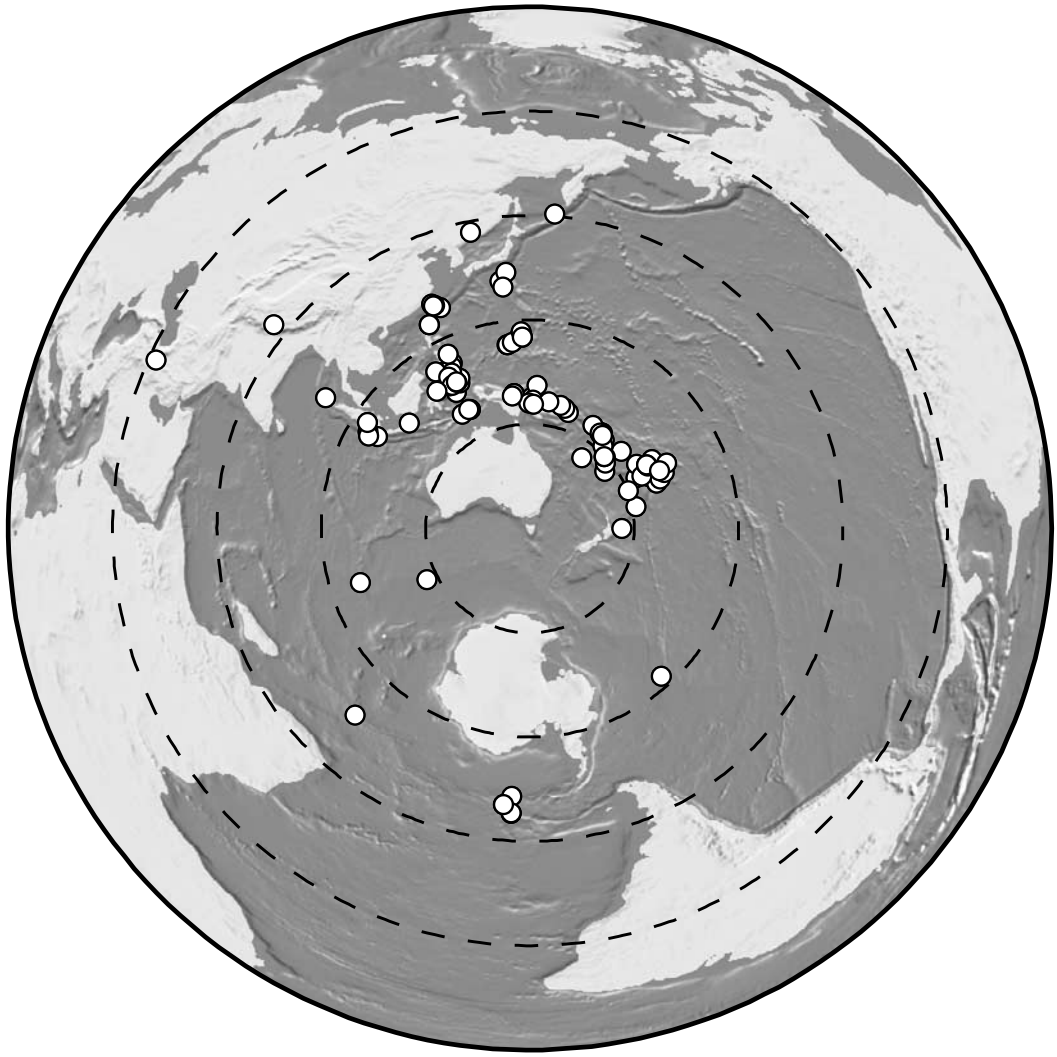

Figure 4. Distribution of the 101 teleseismic events (open circles) used in the tomographic inversion for the 3-D seismic structure beneath northern Tasmania. Dashed circles represent equidistant curves from the center of the TIGGER array contoured at 30° intervals.

characterized by a relatively short sharp pulse on most records. The examples of Figure 5 show a typical cross section of the class of waveforms and signal-to-noise ratios encountered in the TIGGER data set.

4. Relative Arrival Time Residuals

[19] The use of distant earthquake records to constrain the 3-D seismic structure of a local model volume beneath a high-density seismic array has both advantages and disadvantages. In addition to not being able to account for lateral structure outside the 3-D model volume, errors in origin time also mean that the absolute source-receiver travel time should not be used in the inversion. For this reason, teleseismic tomography only exploits the pattern of relative arrival time residuals across the seismic array for each source. An arrival time residual is defined as the difference between an observed and predicted arrival time (using a global reference model). The average event residual is then subtracted to give a relative arrival time residual. Relative arrival time residuals are not significantly affected by errors in source origin time, nor large-scale variations in mantle heterogeneity which may impose a constant offset to the arrival time residual pattern. However, they poorly constrain vertical variations in wave speed, which may lead to erroneous interpretations of the tomographic results [*Lévêque and Masson*, 1999].

[20] An advantage of using distant earthquakes recorded on a local high density seismic network is that, in most cases, the shape of the arriving waveform is relatively invariant across the array. Exploiting this property using cross correlation-type techniques allows arrival time residuals to be picked with high accuracy. One common method for doing this is the multichannel cross correlation (MCCC) technique of *VanDecar and Crosson* [1990], which seeks the least squares solution of an overdetermined system of linear equations formulated from the set of relative time shifts obtained by cross-correlating each trace pair. In an alternative approach, *Chevrot* [2002] uses simulated annealing to minimize a cost function that measures the difference between each recorded trace and a reference

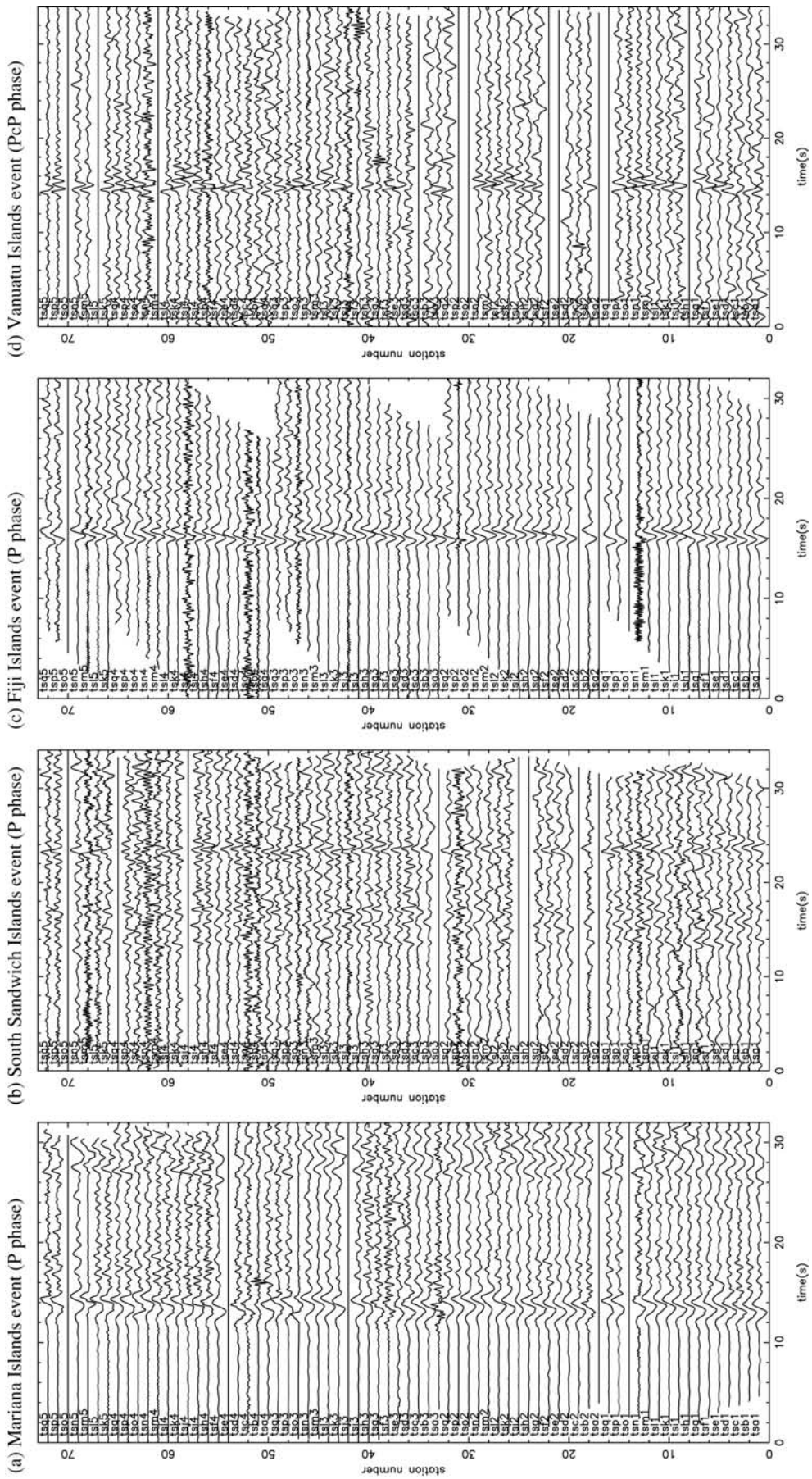

Figure 5. Records from the 72 TIGGER array stations for four different teleseismic events. Trace moveout has been corrected for using the ak135 global reference model. Flat traces denote stations that did not record usable data. (a) The m_b 6.6 event from the Mariana Islands which occurred on 26 April 2002; (b) m_b 5.6 event from the South Sandwich Islands which occurred on 18 April 2002; (c) m_b 6.0 event from the Fiji Islands which occurred on 20 April 2002; and (d) m_b 5.9 event from the Vanuatu Islands which occurred on 27 June 2002.

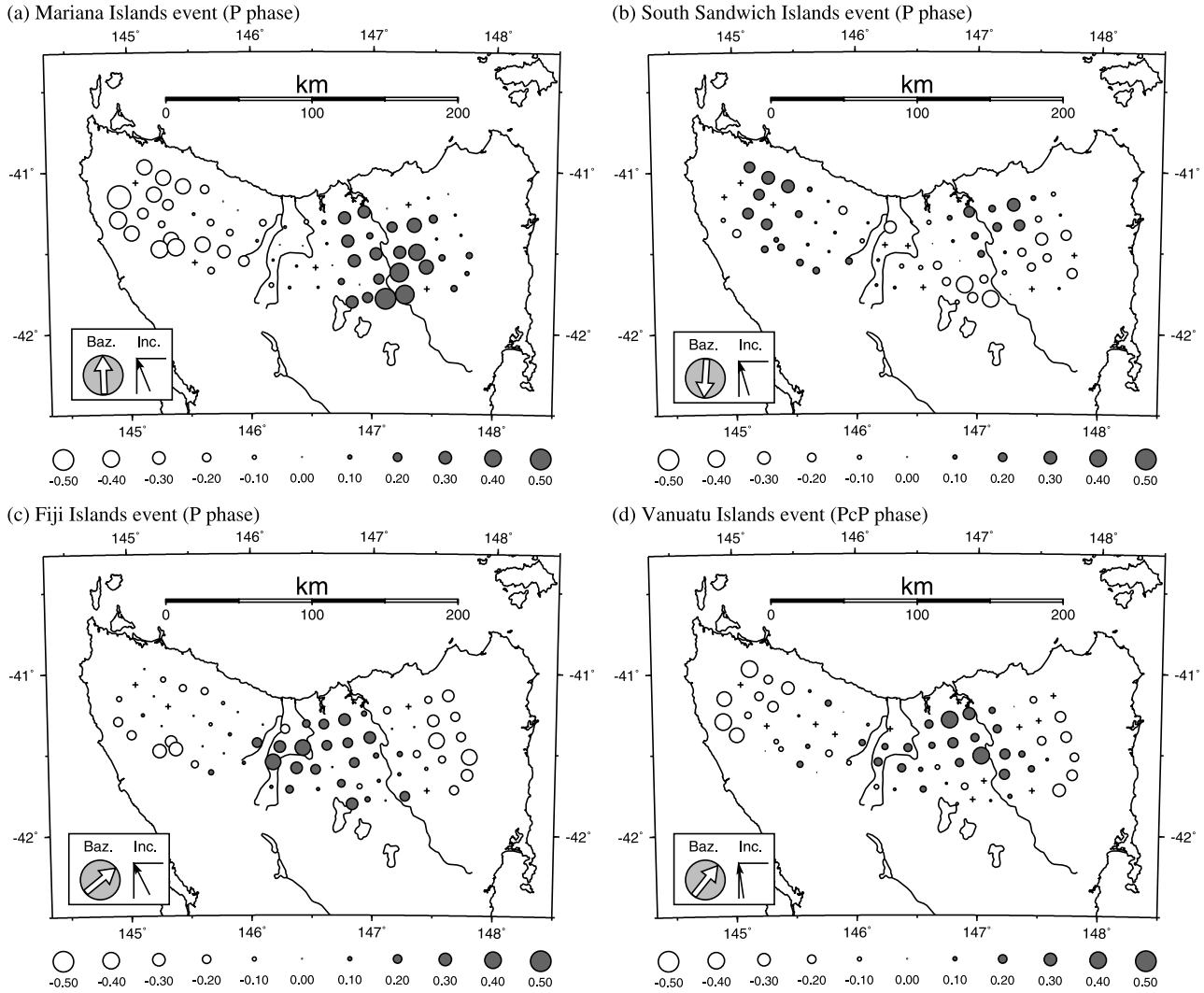

Figure 6. Relative arrival time residual patterns (in seconds) for four different events obtained by aligning the traces shown in Figure 5 using the adaptive stacking technique of *Rawlinson and Kennett* [2004]. Stations which did not record usable data are denoted with a cross. Baz., event back-azimuth; Inc., path inclination.

waveform which can be time delayed. Recently, *Rawlinson and Kennett* [2004] introduced an adaptive stacking technique for obtaining relative and absolute delay times across a network. The approach exploits predictions from a given propagation model to achieve an approximate alignment of traces, which are then stacked to form a reference trace. Iterative improvement of the alignment, by comparison of the reference trace with each station trace, leads to a direct estimate of the residuals and associated picking error. Experiments with teleseismic array data demonstrate the method to be rapid and robust, even in the presence of significant noise and a variety of seismometer responses. For these reasons, we use the adaptive stacking technique to obtain all relative arrival time residuals used in the subsequent inversion results. Note that variations in station elevation are accounted for by the tomographic inversion scheme, so elevation corrections are not made at this stage.

[21] Figure 6 shows arrival time residual patterns for each of the Figure 5 events obtained using the adaptive stacking technique. Despite the presence of traces with no obvious signal, particularly from the South Sandwich Islands event, each of the four maps exhibit a coherent pattern of residuals. This suggests that the adaptive stacking process has been largely successful in matching the coherent component of each trace. Another useful feature of the adaptive stacking scheme of *Rawlinson and Kennett* [2004] is that it automatically generates an uncertainty estimate for each residual. Figure 7 shows the uncertainty estimates associated with each of the four residual maps which comprise Figure 6. A minimum value of 37.5 ms (equal to 75% of the sample interval) is imposed on the uncertainty estimates because it is unrealistic to expect greater accuracy given the presence of noise and imperfect coherence of the waveform across the array.

[22] A preliminary examination of the residual patterns (Figure 6) suggests that Tasmania is underlain by lithosphere with significant lateral variations in *P* wave speed; in the case of the Mariana Islands event (Figure 6a), peak to peak changes in residual size exceed 1 s. Examining

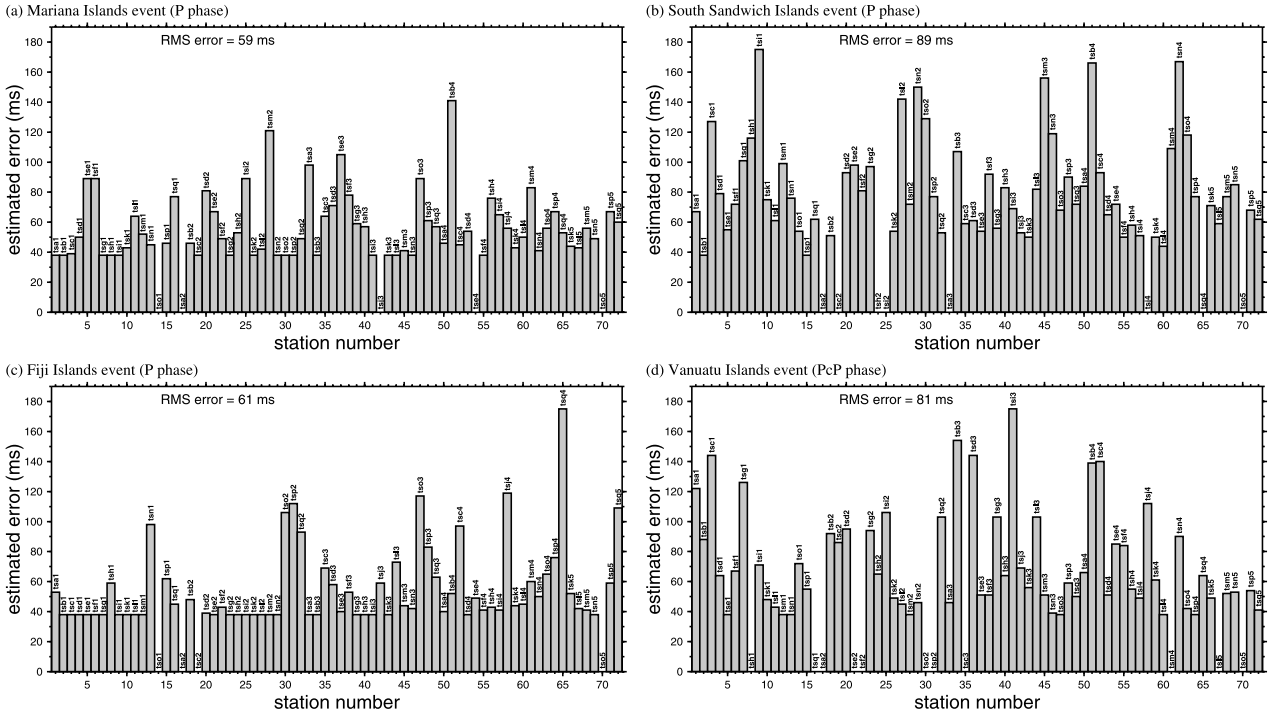

Figure 7. Uncertainty estimates for the relative arrival time residuals shown in Figure 6. Stations that did not record usable data have error estimates set to zero.

Figure 6a in isolation superficially suggests that western Tasmania is underlain by fast lithosphere and eastern Tasmania is underlain by slow lithosphere, with a distinct boundary separating the two. However, the residuals are a path average quantity, so there is a strong dependence on event back-azimuth and angular distance which makes such an inference difficult to substantiate, as demonstrated by the different patterns obtained in Figures 6b–6d. Therefore, to understand the true 3-D nature of the underlying lithosphere, it is necessary to map the residual patterns as perturbations in *P* wave speed using teleseismic tomography.

5. New Tomographic Inversion Method

[23] A new tomographic inversion scheme for teleseismic data has been developed which exploits recent advances in grid-based wave front tracking and uses a fast inversion scheme that is well suited to problems with large numbers of unknowns. The standard ACH approach to teleseismic tomography is to embed a local 3-D model volume that lies beneath the receiver array within a global spherically symmetric reference model. Travel time predictions to the boundary of the local model can then be rapidly calculated before applying more general ray tracing techniques for laterally heterogeneous media.

[24] In the new scheme, 3-D structure beneath the seismic array is represented by a mosaic of cubic B spline volume elements, the values of which are controlled by a mesh of velocity vertices in spherical coordinates. The advantage of a cubic B spline parameterization is that it is everywhere continuous in curvature, is locally controlled by the velocity mesh, and can be easily discretized to any required spatial resolution. Outside the local model volume, the Earth is assumed to be spherically symmetric, which allows rapid computation of travel times. In our case, we use the ttimes software [*Kennett and Engdahl*, 1991] to compute ak135 travel times [*Kennett et al.*, 1995] from the source to the base of the local 3-D model volume.

5.1. Fast Marching Method

[25] The core originality of the new tomographic inversion scheme is its use of FMM to compute travel times from the base of the 3-D model volume to the seismic array on the surface. FMM is a grid based eikonal solver for computing the evolution of monotonically advancing fronts, and has been applied to many areas of the physical sciences, including photolithographic development, geodesics and medical imaging [*Sethian*, 1996, 1999, 2001]. In the field of seismology, FMM has been used in the migration of coincident reflection data [*Sethian and Popovici*, 1999; *Popovici and Sethian*, 2002] and to compute reflection and refraction phases in layered media [*Rawlinson and Sambridge*, 2004a, 2004b]. However, until now, it has not been used in seismic tomography. FMM works by tracking the first-arrival wave front along an evolving narrow band of grid points, the travel time values of which are updated by solving the eikonal equation using upwind entropy satisfying operators.

[26] The entropy satisfying upwind scheme we implement to solve the eikonal equation $|\nabla_{\mathbf{x}} T| = s(\mathbf{x})$ (where T is travel time and s is slowness as a function of the spatial coordinate $\mathbf{x}$) is given by

$$\begin{bmatrix} \max\left(D_a^{-r}T, -D_b^{+r}T, 0\right)^2 \\ +\max\left(D_c^{-\theta}T, -D_d^{+\theta}T, 0\right)^2 \\ +\max\left(D_e^{-\phi}T, -D_f^{+\phi}T, 0\right)^2 \end{bmatrix}^{\frac{1}{2}}_{i,j,k} = s_{i,j,k} \qquad (1)$$

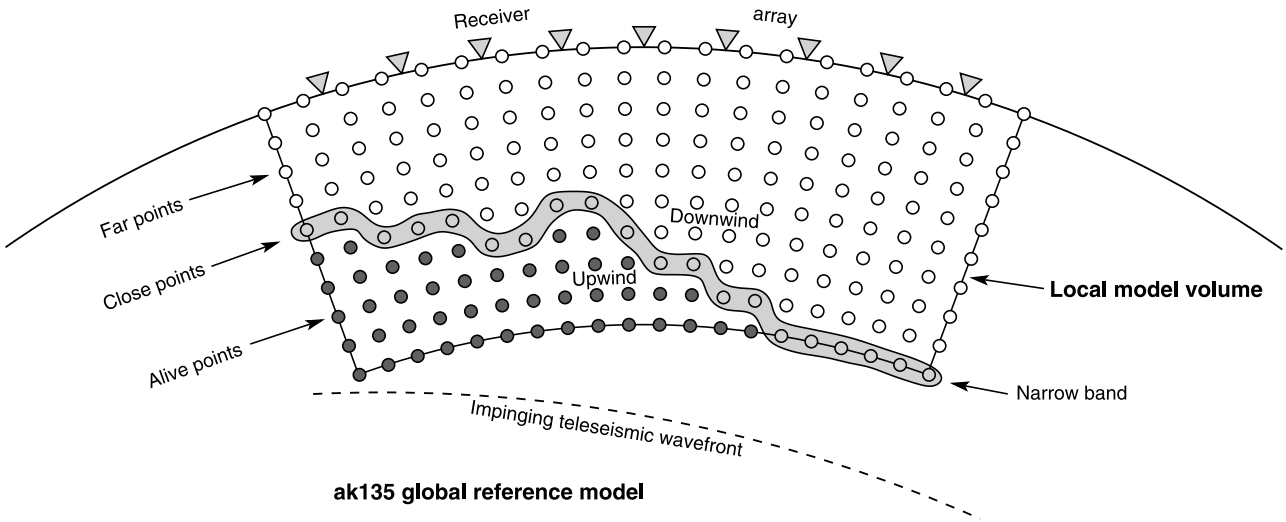

Figure 8. Schematic diagram showing the approach used to calculate travel times. Outside the local model volume, the Earth is assumed to be spherically symmetric, which allows travel times to all grid nodes at the base of the local model to be rapidly computed. FMM is then initiated, with the starting narrow band encapsulating all points on the bottom surface of the model. The narrow band is then evolved through the grid until all points become alive (i.e., they have travel times correctly computed). Close points have trial travel times, and far points are yet to have travel times computed.

where (i, j, k) are spherical grid increment variables in (r, θ, ϕ), and the integer variables a, b, c, d, e, f define the order of accuracy of the upwind finite difference operator used in each of the six cases. For example, the first two upwind operators for $D_e^{-\phi} T_{i,j,k}$ are

$$D_1^{-\phi} T_{i,j,k} = \frac{T_{i,j,k} - T_{i,j,k-1}}{r_i \sin\theta_j \delta\phi}$$
$$D_2^{-\phi} T_{i,j,k} = \frac{3T_{i,j,k} - 4T_{i,j,k-1} + T_{i,j,k-2}}{2r_i \sin\theta_j \delta\phi} \quad (2)$$

where $\delta\phi$ is the grid spacing in ϕ. Which operator is used in equation (1) depends on the availability of upwind travel times. Our mixed-order scheme preferentially uses D_2 operators but reverts to D_1 operators if the second upwind travel time is unavailable.

[27] The order in which node travel times are updated using equation (1) must be consistent with the direction of flow of information, that is, from smaller to larger values of T. This is achieved by systematically constructing travel times in a downwind fashion from known values upwind using a narrow band approach (see Figure 8). All grid points are labeled as either "alive," "close," or "far." Alive points lie upwind of the narrow band and have correct travel time values; close points lie within the narrow band and have trial values computed from equation (1) using alive points only; far points lie downwind of the narrow band and have no travel time values calculated. The narrow band is evolved by identifying the close point with minimum travel time (using a heap sort algorithm), tagging it as alive, and then tagging all neighboring far points as close. Finally, all close points adjacent to the new alive point have their travel times updated using equation (1). The use of a heap sort algorithm means that FMM has an operation count of O(N log N), where N is the total number of grid points. The resulting scheme is both fast and highly stable, a combination that makes it particularly attractive for large tomographic problems, where both speed and robustness are essential.

[28] For use in our teleseismic tomography routine, we initialize the narrow band from the bottom surface of the local model beneath the array, where initial travel times have been provided by the global reference model ak135. Ray paths, which are required in order to estimate the Fréchet derivatives for the inversion step, are computed by following the travel time gradient from the receiver to the base of the model. The velocity grid required by FMM is obtained by discretizing the cubic B spline velocity field at the desired resolution. Since the computing time of FMM scales as O(N log N), it is important to choose the grid spacing (about 3 km in our case) which produces the largest acceptable travel time error in order to achieve maximum computational efficiency.

[29] Compared to conventional ray tracing schemes, which are normally used in teleseismic tomography [e.g., *VanDecar*, 1991; *Steck et al.*, 1998], FMM has several potential advantages. First and foremost, it is highly robust, and is capable of always converging to the correct high-frequency solution as the grid spacing is reduced, even in very complex media [*Sethian and Popovici*, 1999; *Rawlinson and Sambridge*, 2004a]. Both shooting and bending methods of ray tracing can fail to converge on true two point paths, even in the presence of relatively simple velocity structures [e.g., *Kim and Baag*, 2002]. Another advantage of FMM is that it consistently locates the first arrival; in general, there is no guarantee with ray tracing as to whether the first or a later arrival has been located. Finally, FMM can be more computationally efficient than ray tracing, particularly if there are many more sources than receivers or vice versa [*Rawlinson and Sambridge*, 2004a, 2004b].

5.2. Subspace Inversion Scheme

[30] The final step of the tomographic imaging scheme is to solve the inverse problem, which requires the adjustment of model parameters in order to satisfy the data, subject to regularization constraints. In our case, the data are the relative arrival time residuals, and the unknowns are the grid of vertices that control the pattern of the B spline velocity field. The inverse problem can be solved by specifying an objective function $S(\mathbf{m})$, where $\mathbf{m}$ are the model parameters, which is to be minimized. Here, we use an objective function of the form

$$S(\mathbf{m}) = \big(\mathbf{g}(\mathbf{m}) - \mathbf{d}_{\text{obs}}\big)^{\mathrm{T}}\mathbf{C}_{\mathrm{d}}^{-1}\big(\mathbf{g}(\mathbf{m}) - \mathbf{d}_{\text{obs}}\big) + \epsilon(\mathbf{m} - \mathbf{m}_0)^{\mathrm{T}}\mathbf{C}_{\mathrm{m}}^{-1}(\mathbf{m} - \mathbf{m}_0) + \eta\mathbf{m}^{\mathrm{T}}\mathbf{D}^{\mathrm{T}}\mathbf{D}\mathbf{m} \quad (3)$$

where $\mathbf{g}(\mathbf{m})$ are the predicted residuals, $\mathbf{d}_{\text{obs}}$ are the observed residuals, $\mathbf{C}_{\mathrm{d}}$ is the a priori data covariance matrix, $\mathbf{m}_0$ is the reference model, $\mathbf{C}_{\mathrm{m}}$ is the a priori model covariance matrix, and $\mathbf{D}$ is a second derivative smoothing operator. ϵ and η are known as the damping parameter and smoothing parameter respectively, and govern the trade-off between how well the solution satisfies the data, the proximity of the solution model to the starting model, and the smoothness of the solution model.

[31] We use an iterative nonlinear approach in order to minimize equation (3), which successively applies a mixed-order FMM scheme to solve the forward problem and a subspace inversion method [*Kennett et al.*, 1988] to solve the linearized inverse problem. Thus, for some current model $\mathbf{m}_i$, a new model $\mathbf{m}_{i+1} = \mathbf{m}_i + \delta\mathbf{m}_i$ is produced where the model perturbation $\delta\mathbf{m}_i$ is supplied by the subspace inversion method. The scheme progresses until the observed data are satisfied or when the change in $S(\mathbf{m})$ with iteration gets sufficiently small. The use of an iterative approach means that the nonlinear relationship between travel time and velocity structure is accounted for.

[32] Subspace inversion methods are rarely used in seismic tomography, with the notable exception being several controlled source studies [*Sambridge*, 1990; *Williamson*, 1990; *Wang and Houseman*, 1995; *Rawlinson et al.*, 2001a], which generally did not involve a large number of unknowns. Given that our tomographic problem is different, and that we use a different form of objective function and selection process for the projection matrix, a brief description of the subspace scheme we implement is given below.

[33] The subspace inversion method works by projecting the quadratic approximation of $S(\mathbf{m})$ onto an n-dimensional subspace of model space. For an objective function of the form of equation (3), the perturbation $\delta\mathbf{m}$ is given by [see *Rawlinson and Sambridge*, 2003, for a derivation]

$$\delta\mathbf{m} = -\mathbf{A}\big[\mathbf{A}^{\mathrm{T}}\big(\mathbf{G}^{\mathbf{T}}\mathbf{C}_{\mathrm{d}}^{-1}\mathbf{G} + \epsilon\mathbf{C}_{\mathrm{m}}^{-1} + \eta\mathbf{D}^{\mathrm{T}}\mathbf{D}\big)\mathbf{A}\big]^{-1}\mathbf{A}^{\mathrm{T}}\hat{\boldsymbol{\gamma}} \quad (4)$$

where $\mathbf{A} = [\mathbf{a}^j]$ is the $M \times n$ projection matrix (for M unknowns), $\mathbf{G}$ is the matrix of Fréchet derivatives and $\hat{\boldsymbol{\gamma}}$ is the gradient vector ($\boldsymbol{\gamma} = \partial S/\partial\mathbf{m}$). The basis vectors that span the n-dimensional subspace are in our case based on the gradient vector in model space $\boldsymbol{\gamma} = \mathbf{C}_{\mathrm{m}}\hat{\boldsymbol{\gamma}}$ and the model space Hessian $\mathbf{H} = \mathbf{C}_{\mathrm{m}}\hat{\mathbf{H}}$, where $\hat{\mathbf{H}} = \partial^2 S/\partial\mathbf{m}^2$. The first search direction is given by $\mathbf{a}^1 = \boldsymbol{\gamma}$, the direction of steepest ascent. All subsequent search directions are given by $\mathbf{a}^{j+1} = \mathbf{H}\mathbf{a}^j$ (for $j = 2, \ldots$), which means that $\mathbf{a}^{j+1}$ is based on the rate of change of $\mathbf{a}^j$. In order to avoid linear dependence between different $\mathbf{a}^j$, singular value decomposition (SVD) is used to produce an orthonormal basis [*Press et al.*, 1992]. For large n, the set of $\mathbf{a}^j$ may not completely span all n dimensions. In such cases, SVD can identify the unnecessary basis vectors so that they can be removed from $\mathbf{A}$. In all subsequent calculations, we use a subspace dimension of 10, but allow our SVD algorithm to dynamically remove unnecessary basis vectors at each iteration. Therefore, in practice, the subspace dimension tends to vary between 7 and 10 from iteration to iteration.

[34] Once the projection matrix $\mathbf{A}$ has been computed and orthonormalized, the model update $\delta\mathbf{m}$ is rapidly obtained by the inversion of a relatively small $n \times n$ matrix. The subspace inversion method is extremely stable and efficient for large underdetermined inverse problems, and together with FMM, forms the basis of a fast and robust tomographic imaging scheme.

6. Results

[35] In order to represent seismic structure in the crust and upper mantle beneath the TIGGER array, we define a local model volume comprising 61,380 velocity nodes at approximately 10 km spacing in all three dimensions (latitude, longitude and depth). The model spans 190 km in depth, 3.78° in latitude and 7.08° in longitude. The 1-D reference or starting model for the inversion is based on velocity values obtained from a refraction and wide-angle reflection experiment carried out in Tasmania in 1995 [*Rawlinson et al.*, 2001a, 2001b]. However, since ray coverage in this study is limited to the crust and uppermost mantle, the ak135 global reference model is used to define velocities below approximately 50 km in depth. It is worth noting that since the data only constrain relative perturbations in wave speed, the ray path distribution will have a dependence on the starting model even in a nonlinear inversion. Although, according to Fermat's principle, this effect is second order, it does suggest that highly inaccurate starting models may unduly influence the resulting pattern of velocity perturbations. Given that global reference models such as ak135 are least accurate in the crust and uppermost mantle, we felt it important to incorporate locally obtained crustal velocity information in our starting model.

[36] A total of 6520 relative arrival time residuals from 101 teleseismic sources are used as input data to the inversion. In addition, error estimates from the adaptive stacking picking routine are used in the diagonal elements of $\mathbf{C}_{\mathrm{d}}$ to weight the relative importance of each residual in the inversion. The a priori model uncertainty associated with each velocity node, which is used to form the diagonal elements of $\mathbf{C}_{\mathrm{m}}$, is set to 0.3 km/s. However, since the damping factor ϵ is varied to tune the inversion, the a priori velocity uncertainty we choose is relatively unimportant. Note that stations are positioned at their correct elevation when solving the forward problem so that the predicted and observed travel time residuals are correctly matched.

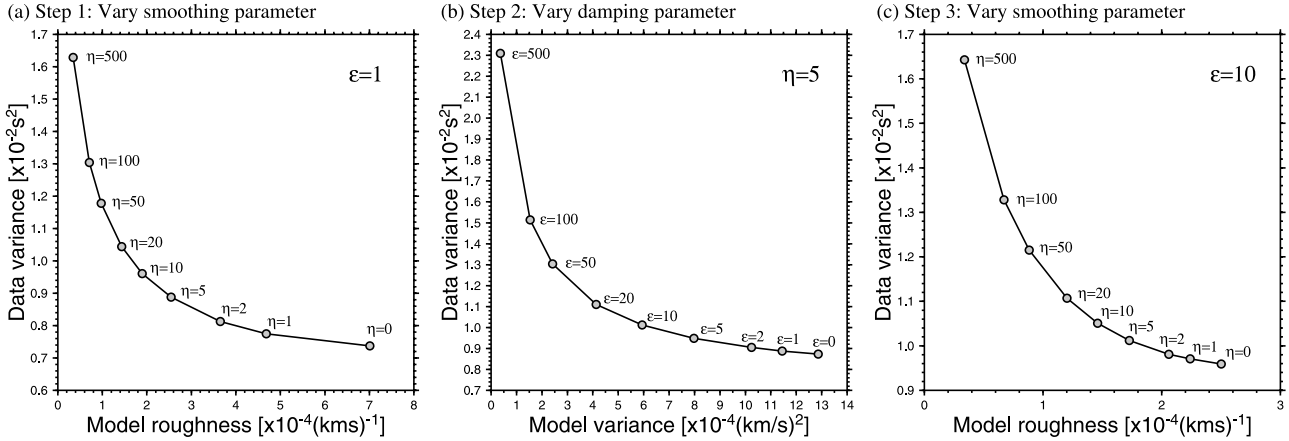

Figure 9. Scheme used to estimate optimum damping and smoothing parameters. (a) Vary smoothing parameter while holding damping parameter fixed at $\epsilon = 1$. In this case, $\eta = 5$ is chosen from the curve. (b) Vary damping parameter while holding smoothing parameter fixed at $\eta = 5$. The value $\epsilon = 10$ is chosen as optimum, although $\epsilon = 20$ would also be a good choice. (c) Vary η while holding the damping parameter fixed at the new value of $\epsilon = 10$. The value $\eta = 5$ still appears to be an acceptable choice.

[37] The complete inversion procedure is carried out using six iterations of a 10-D subspace inversion routine (noting from section 5 that the actual subspace dimension at each iteration may be less than 10) with $\epsilon = 10$ and $\eta = 5$. The forward problem is solved between each iteration to obtain new travel times, ray paths and Frechét derivatives. The CPU time for the complete process is approximately 20 min on a 1.6 GHz Opteron workstation running Linux. The forward problem takes 3 minutes to compute, while the inverse problem only takes 9 seconds.

[38] The appropriate trade-off between fitting the data and satisfying the regularization constraints was obtained by running the complete inversion process a number of times with different values of ϵ and η. This was done systematically by first setting the damping parameter to $\epsilon = 1$ and varying η. Figure 9a shows a plot of the resultant trade-off between the residual data variance and roughness of the solution model. From this curve, we chose $\eta = 5$ as offering the best trade-off between minimizing the data misfit and producing the smoothest model. In the next step, the smoothing parameter was set to $\eta = 5$ and ϵ was varied. The trade-off curve generated from this process (Figure 9b) suggests that $\epsilon = 10$ produces a model that satisfies the data to nearly the same extent as models produced with lower ϵ values, but with significantly smaller perturbations in velocity. Finally, since ϵ and η both affect model variance and roughness, the first step was repeated with $\epsilon = 10$. The resulting trade-off curve (Figure 9c) shows that $\eta = 5$ is still a good choice of smoothing parameter, making further iterations of this process unnecessary.

[39] The final solution model reduces the data variance by 74% from 0.0375 s^2 to 0.0097 s^2, which corresponds to an RMS reduction from 193.7 ms to 98.7 ms. The reduction in data variance due to structure alone (i.e., excluding variations in elevation) is 67%. The estimated standard deviation of the data noise is 77 ms, which indicates that the inversion has done an acceptable job in fitting the data. The remaining misfit can be attributed to a number of factors including shallow crustal structure (which is often highly variable) and mantle structure beneath the local model volume, neither of which can be resolved by the data. In the latter case, it is worth noting that the surface wave tomography study of *Fishwick et al.* [2005] does not indicate the presence of any major sublithospheric anomalies that may significantly affect our imaging results. Histograms showing the distribution of all relative arrival time residuals for the initial and final models are shown in Figures 10a and 10b, respectively.

6.1. Robustness of Tomography

[40] Before presenting tomographic images from the inversion of the TIGGER data set, the extent to which the model parameters are constrained by the data is first investigated. Ultimately, the inverse problem that we solve is underdetermined and the solution nonunique, as a variety of different models will satisfy the data to the same extent. This is due largely to variable path coverage and data uncertainty. It is therefore important to gain an understanding of which features of the model are required by the data and which are not. In gradient-based seismic tomography, two common approaches for doing this are synthetic resolution tests, and estimating posteriori model covariance and resolution by assuming local linearity [*Rawlinson and Sambridge*, 2003].

[41] We choose to use synthetic tests to analyze the robustness of our solution model. This involves using the identical sources, receivers and phases types of the observational data set to predict the travel time residual patterns for a given structure. These data are then inverted using the tomographic procedure outlined above; the difference between the synthetic and recovered structures gives an indication of which regions of the model are well constrained by the data.

[42] The first set of synthetic tests involves the so-called ''checkerboard test'', in which the synthetic model is divided into alternating regions of high and low velocity with a scale length approximately equal to the smallest wavelength structure recovered in the solution model. Regions in which the checkerboard pattern is clearly recovered can be considered well resolved. This class of

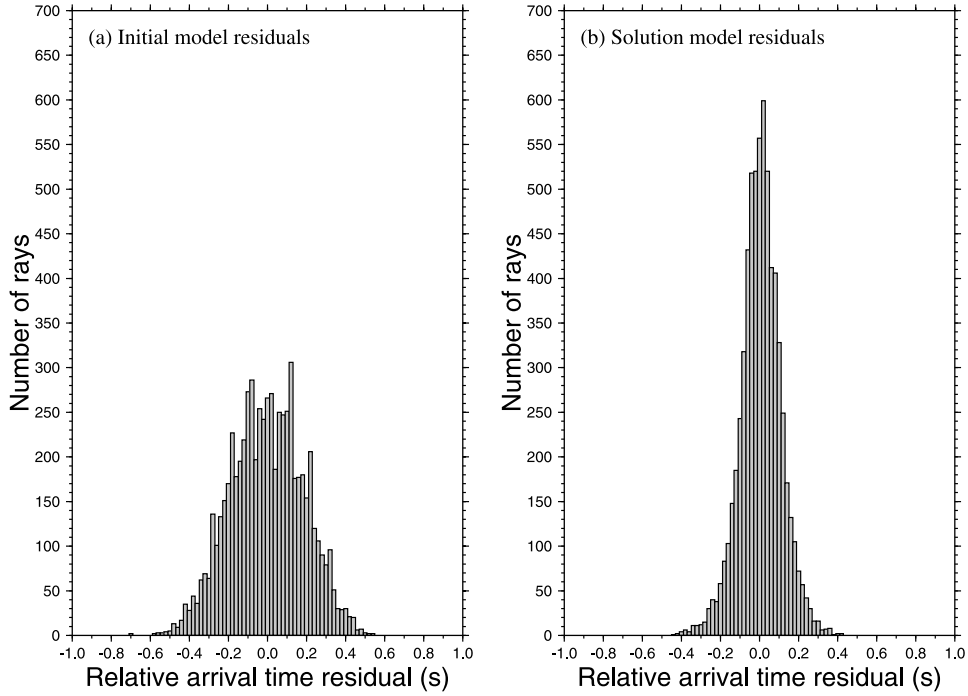

Figure 10. Magnitude and distribution of relative arrival time residuals for the initial and solution model.

test is frequently used to assess the solution of large tomographic problems [e.g., *Achauer*, 1994; *Seber et al.*, 1996; *Zelt and Barton*, 1998; *Graeber et al.*, 2002]. However, it is possible for the small-scale structure of the checkerboard to be well retrieved while larger-scale structure is poorly retrieved [*Lévêque et al.*, 1993]. To address this problem, we use three synthetic models with different sized checkerboards (see Figure 11), which are classified as (1) coarse (~50 km scale length) (Figure 11, left), (2) intermediate (~30 km scale length) (Figure 11, middle), and (3) fine (~20 km scale length) (Figure 11, right). In all cases, the checkerboard varies in latitude, longitude and depth.

[43] Gaussian noise with a standard deviation of 77 ms is added to all three synthetic data sets to simulate the noise content of the observed data. Horizontal and vertical slices through the recovered models are shown in Figure 12 (compare Figure 11). The path coverage effects of the azimuthal distribution of sources (Figure 4) are evident in the recovered patterns. In particular, the smearing of anomalies present in the E-W (Figure 12b) and N-S (Figure 12c) slices is mainly due to the high concentration of events to the north and east of the array and the low concentration to the south and west. Despite these effects, significant regions of the model recover the checkerboard pattern, although in general the amplitude of the perturbations are underestimated. In addition, the region of good recovery is larger for the coarse checkerboard model than the fine checkerboard model; this behavior is to be expected since decreasing path density increases the minimum scale length of resolvable structure. For example, if we compare Figures 12a (left) and 12a (right), the checkerboard pattern can be observed as far south as central Tasmania in the former case, but only as far south as the center of the array in the latter case. Thus there are enough rays from the south to resolve large-scale structure, but not enough to resolve the small-scale structure of the fine checkerboard.

[44] One potential complication of applying checkerboard resolution tests to teleseismic data is that when anomalies are smeared along predominant ray trajectories, they tend to merge with diagonally adjacent anomalies of the same sign (e.g., Figure 12c). This makes it difficult to gauge the actual extent to which each cell is smeared. Therefore another type of test, in which short scale length anomalies are sparsely distributed throughout the model volume, is carried out.

[45] Figure 13 shows a series of cross sections through a synthetic and recovered model comprising six anomalies of identical amplitude and dimensions to the cells of the intermediate checkerboard model (e.g., Figure 11a (middle)). In general, the solution model manages to recover the input anomalies, although in all cases there are varying levels of spatial distortion. Note that the presence of low amplitude background "noise" in the recovered model can be attributed to the Gaussian noise added to the synthetic data set. The low-velocity anomaly at 42.1°S is the most poorly recovered of the six, as it is barely discernable above the background noise in all three cross sections (Figure 13a (bottom right), 13b (bottom right), and 13c (bottom middle)). This can be attributed to a lack of good path coverage from the south and south west. There is also a tendency to smear structure lying to the north of the array along predominant ray directions as shown in Figure 13c (bottom left) and 13c (bottom right); in both cases the recovered anomaly has been elongated by a factor of about 2.5.

6.2. Tomographic Model

[46] Cross sections through the solution model obtained by inversion of the TIGGER data set are shown in Figure 14 and reveal a number of significant structural features. The

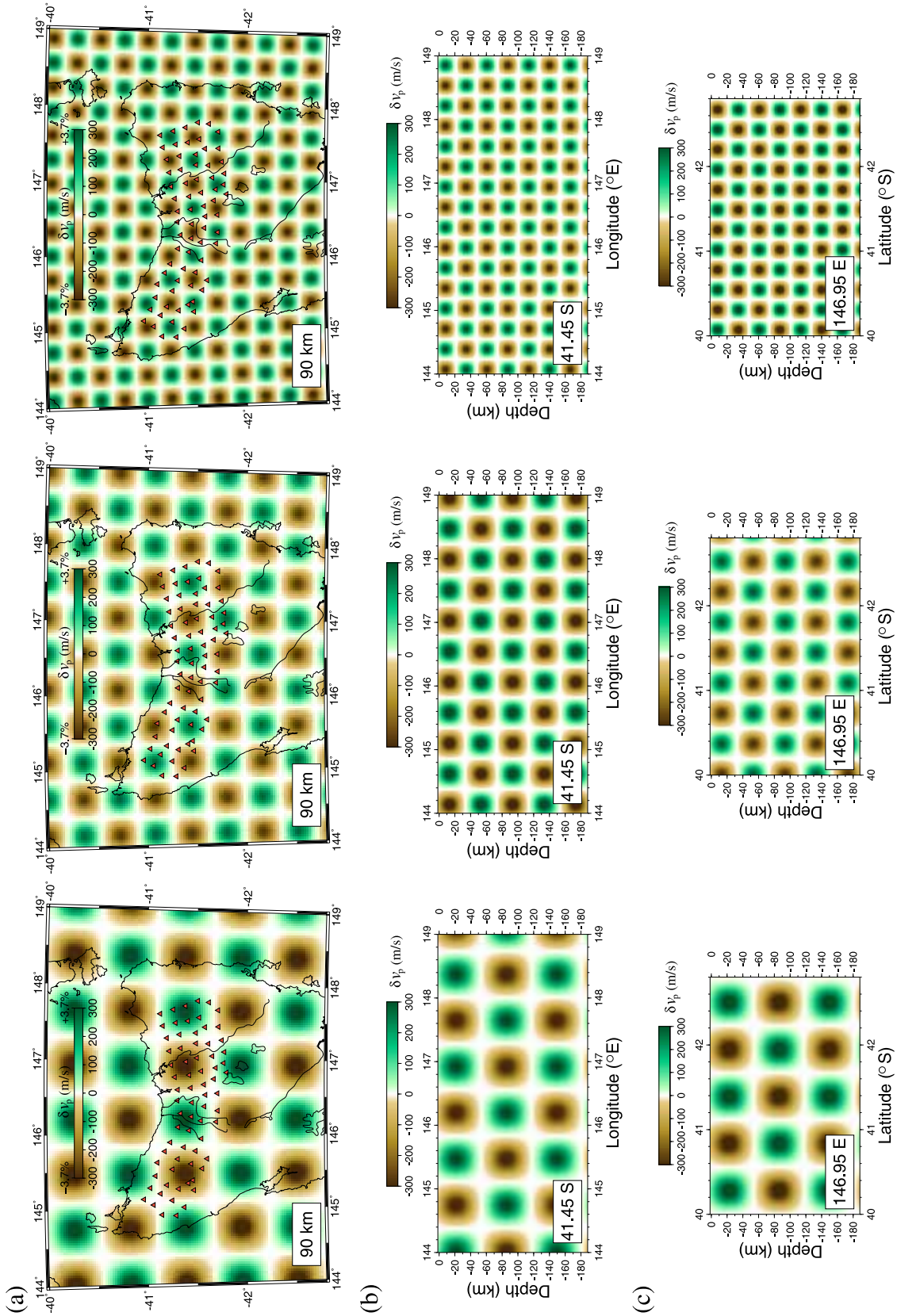

Figure 11. Input checkerboard models for synthetic tests. (a) Depth slices; (b) E-W slices; and (c) N-S slices. Three models with different scale lengths are used to analyze the resolving power of the data set. (left) Coarse model; (middle) intermediate model; and (right) fine model. Note that E-W and N-S cross sections in this and all subsequent figures are free from vertical exaggeration.

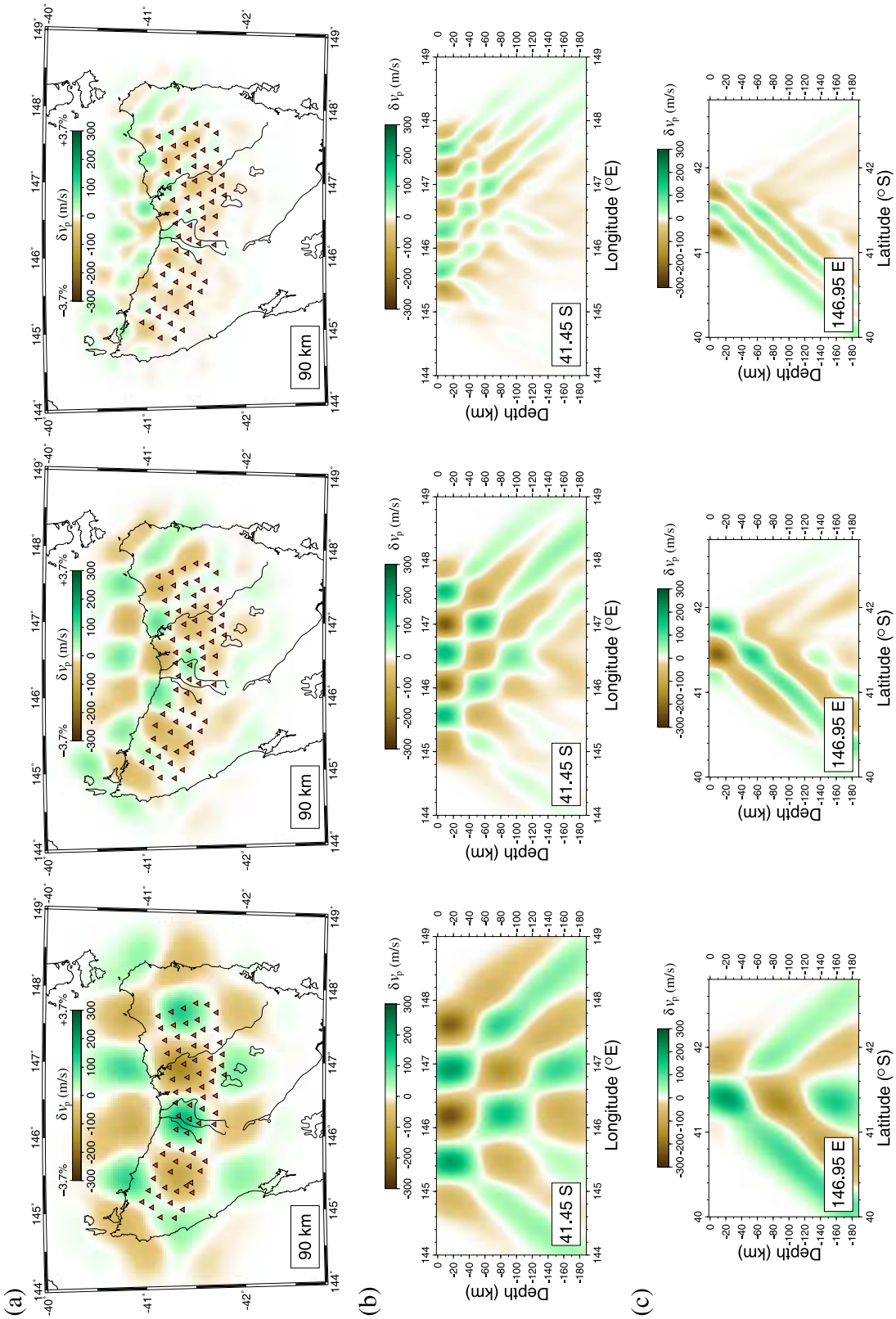

Figure 12. Recovered checkerboard models obtained by inverting synthetic data sets. (a) Depth slices; (b) E-W slices; and (c) N-S slices. Compare to Figure 11.

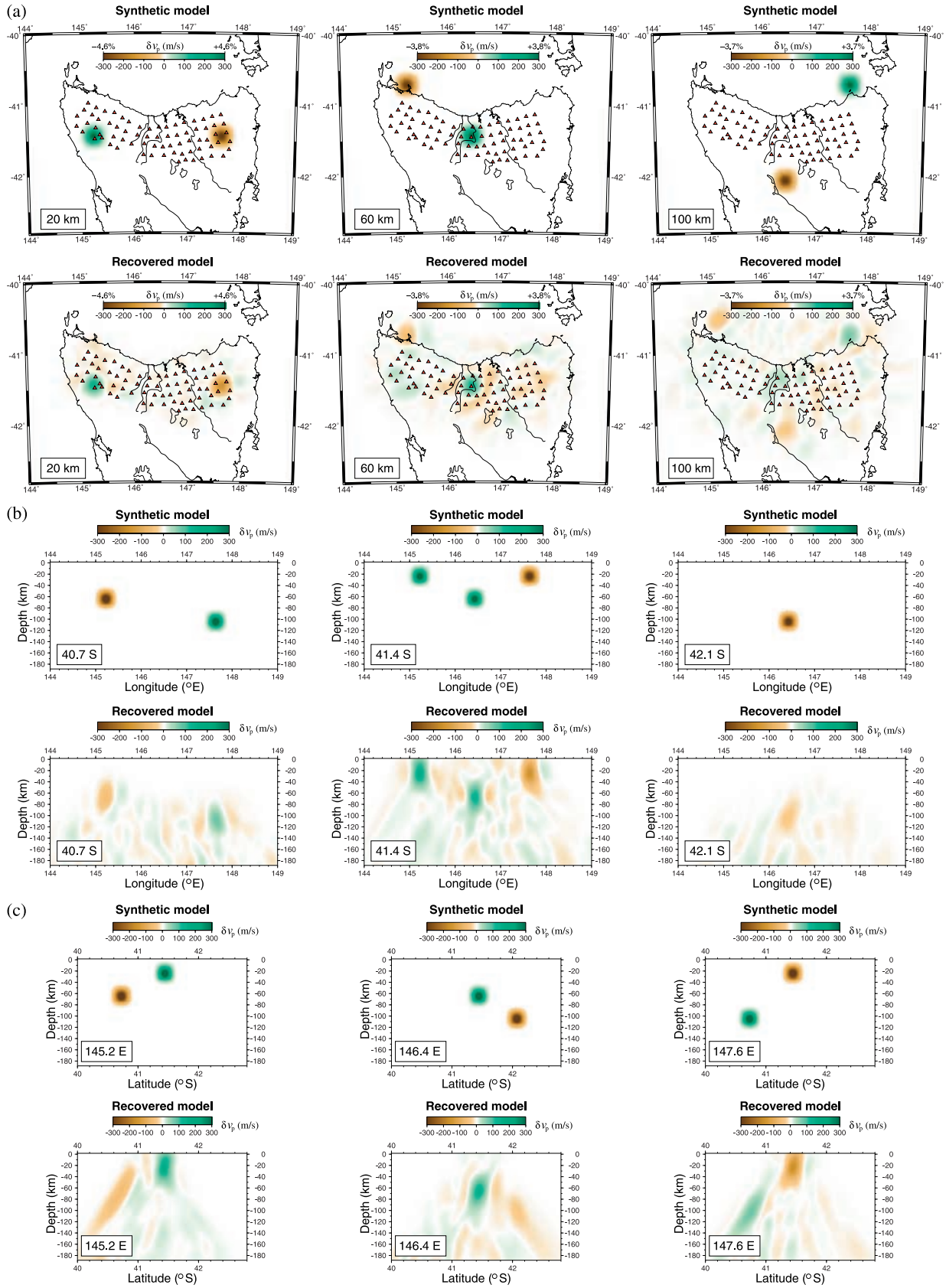

Figure 13. Synthetic test results involving the recovery of six sparsely separated anomalies. (a) Depth slices; (b) E-W slices; and (c) N-S slices.

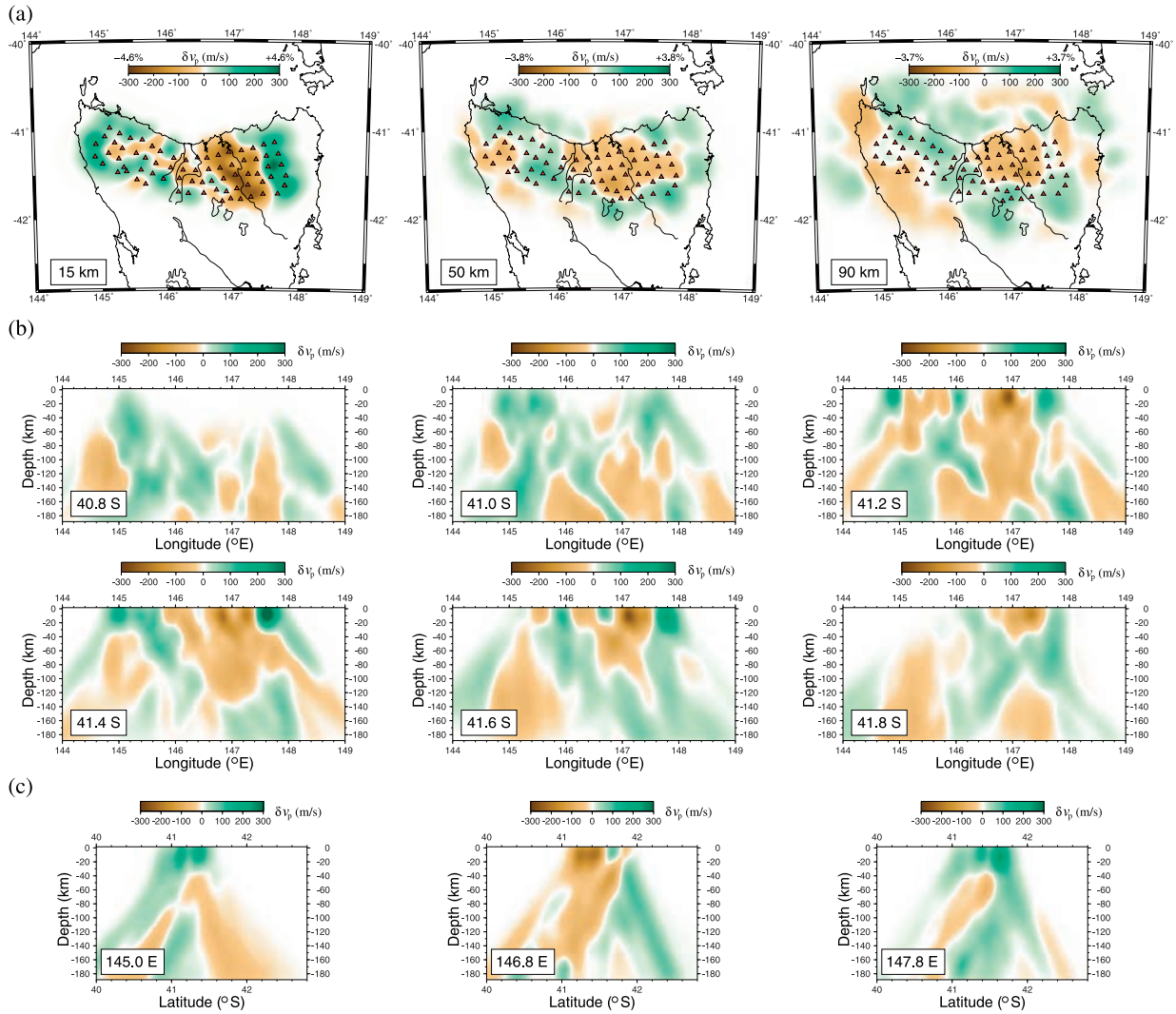

Figure 14. Horizontal and vertical slices through 3-D solution model obtained by inversion of TIGGER data set. (a) Depth slices; (b) E-W slices; and (c) N-S slices.

horizontal slice at 15 km depth (Figure 14a, left) shows a coherent pattern of relative crustal velocities, which varies from fast to slow to fast from east to west. The variation from fast to slow in the east is particularly prominent, with the decrease in velocity as large as 0.5 km/s over about 10 km. It is notable that although this pattern persists through the crust, it is no longer present in the uppermost mantle (Figure 14a, right). This can also be clearly observed in north-south cross sections (Figure 14c), even taking into account the structural smearing that is known to exist from the resolution tests.

[47] The east-west cross sections (Figure 14b) are approximately perpendicular to the strike of the predominant surface geology. Because of the geometry of the array, there is little recovery of shallow structure east of 146°E in Figure 14b (top left), between 146°E and 147°E in Figure 14b (top middle), and west of 146°E in Figure 14b (bottom right). Nevertheless, there are some significant structural trends that span most of these cross sections. These are perhaps most clear in Figure 14b (bottom left), which is a slice at 41.4°S. The east-west fast-slow-fast variation in relative crustal velocity is clearly evident, but there also exists an eastward dipping zone of elevated velocity emanating from the high-velocity crustal zone in the west that extends into the mantle. To the east of this structure is a "core" of relatively low velocity which extends beneath the high-velocity crust east of the Tamar river. Figure 15 shows the slice at 41.4°S with these features highlighted.

[48] E-W cross sections adjacent to Figure 15 show similar features; for example, Figures 14b (top right) and 14b (bottom middle) contain an easterly dipping structure and central zone of relatively low velocity, although in the latter case the low-velocity zone is smaller. Farther south at 41.8°S (Figure 14b, bottom right), the low-velocity zone is limited to shallow depths and there is no evidence for an easterly dipping zone of relatively high velocity. However, this is not surprising given the lack of resolution west of 146° in this part of the model. While there is some evidence for easterly dipping high-velocity structures in the slices at 40.8°S and 41.0°S (Figures 14b (top left) and 14b (top middle), respectively), the lack of data coverage at shallow

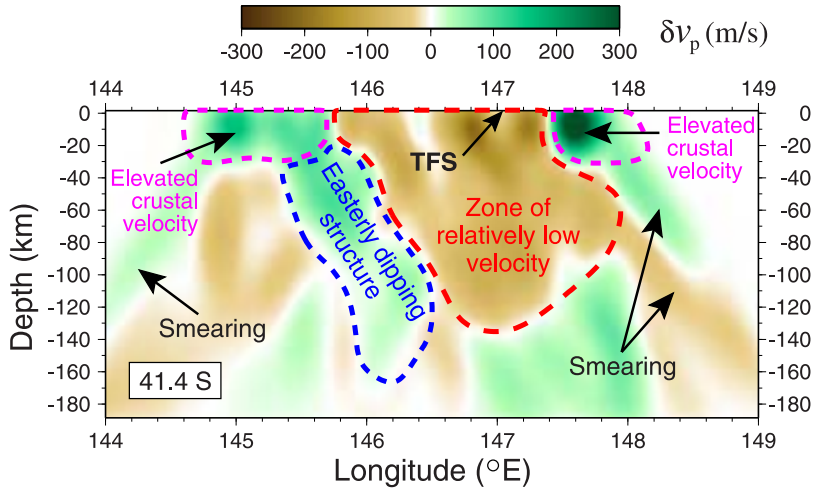

Figure 15. E-W slice through the solution model with several features of interest highlighted. Note that the Tamar Fracture System (TFS) does not overlie any significant velocity transition.

depths makes it difficult to identify a northward extension of the low-velocity zone.

7. Discussion

7.1. Constraining Crustal Structure

[49] The resolution test results summarized in Figures 12 and 13 clearly show that the TIGGER data set is capable of resolving mid-lower crustal structures with scale lengths as small as 20 km. However, the Earth's crust is typically complex and can contain large variations in wave speed over small distances, due to features such as faults, thrusts and folds which cause material displacement, sedimentary basins, igneous intrusions and so forth. The presence of such small-scale complexities will influence the travel times of teleseismic waves, but because of data coverage and finite frequency considerations, they usually cannot be correctly mapped as structure by the tomographic inversion. An additional complication is the presence of an undulating Moho, which will influence relative arrival time residual patterns. Teleseismic tomography based on continuous velocity parameterization is likely to misrepresent these variations in interface depth as variations in wave speed within the crust.

[50] Several approaches have been developed to try and account for the component of arrival time residuals caused by unresolvable shallow structure. One of the most common is to include station terms as unknowns in the inversion, the idea being that the influence of local structure beneath each receiver can be removed by attributing it to an unknown travel time perturbation [e.g., *Frederiksen et al.*, 1998; *Graeber et al.*, 2002]. However, the resulting station corrections are heavily dependent on the regularization imposed on the inversion, and it is possible that travel time residual information caused by resolvable structure will map into the station terms.

[51] A more robust technique that is becoming increasingly common is to use a priori crustal models to correct arrival time residuals for the presence of shallow structure that cannot be resolved by teleseismic data [*Waldhauser et al.*, 2002; *Shomali et al.*, 2002; *Lippitsch et al.*, 2003]. This approach is generally applied to regions where an accurate crustal model exists and the station spacing is large enough that there are no crossing paths within the crust.

[52] The situation in northern Tasmania is complicated by the fact that the data coverage allows mid-lower crustal velocities to be resolved, so we do not wish to try and decouple the arrival time residuals into crust and mantle components. In addition, no detailed crustal model for northern Tasmania exists. A Moho depth model for Tasmania was constructed by *Rawlinson et al.* [2001b] from wide-angle travel times, but data coverage was insufficient to resolve any structure in central and northeast Tasmania. Shallowing of the Moho is observed in northwest Tasmania, which implies that the higher crustal velocities observed in this region in Figure 14 are at least partly caused by thinner crust. However, the Moho model does assume that velocity within a layer is laterally invariant, so the reverse may also be true. In summary, we feel that the presence of shallow crustal velocity variations and Moho undulations are unlikely to cause significant artifacts in our tomographic results, although it would be desirable at some later date to try and simultaneously invert the teleseismic and wide-angle data for velocity and interface structure.

7.2. Geological Implications

[53] The tomographic results from the TIGGER experiment allow a number of important inferences to be made about the geology and tectonic evolution of Tasmania and its relationship with mainland eastern Australia. One of the most obvious features of the tomographic model is the strong contrast in velocity at shallow depths beneath the eastern end of the array (e.g., Figures 14a (left) and 15). The change from significant negative to significant positive perturbations occurs along a narrow zone that runs approximately parallel to, but between 30–40 km east, of the Middle Devonian Tamar Fracture System (Figure 15). This result challenges the notion that a crustal-scale suture zone follows the course of the Tamar river and extends south to near Hobart [*Williams*, 1989]. Rather, it suggests that a profound change in crustal properties occurs farther

to the east, a result that largely agrees with the model proposed by *Reed* [2001].

[54] In this model [see *Reed*, 2001, Figure 6], there is no requirement for Middle Devonian crustal-scale suturing synchronous with the Tabberabberan Orogeny. Instead, it is proposed that the East and West Tasmania terranes were passively joined as far back as the Ordovician, the former underlain by oceanic basement, the latter by Proterozoic siliciclastic crust. Silurian and Early Devonian orogenic episodes, with intervening sediment deposition, significantly deformed the oceanic crust, but had little effect on the continental crust. A final phase of folding in the Middle Devonian deformed the eastern edge of the Proterozoic basement, revealing the so-called Tamar Fracture System as a shallow feature unrelated to the change from Proterozoic continental to younger oceanic crust at depth. The only real disagreement between this model and our tomographic results is that *Reed* [2001] positions the change from Oceanic to Paleozoic continental basement west of the Tamar River. However, the idea that eastern Tasmania is underlain by mafic oceanic crust and western Tasmania is underlain by siliciclastic Proterozoic crust of continental origin correlates well with the relative variations in wave speed seen in the tomographic images.

[55] As discussed in section 2, various scenarios have been put forward to explain the tectonic evolution of western Tasmania during the Middle to Late Cambrian Tyennan Orogeny. One of the more generally accepted of these [*Crawford et al.*, 2003] features easterly dipping subduction which produces an intraoceanic volcanic arc that is subsequently obducted westward by arc-continent collision. The easterly dipping higher velocity structures observed in the tomographic model (Figure 15) may represent remnants of this subduction center that have been frozen into the lithosphere. The question of whether such remnants can be preserved relatively intact over a period of 500 Ma, given the effects of subsequent deformation events and chemical alteration, remains. However, in the case of western Tasmania, there have been no major tectonic adjustments since the Tyennan Orogeny, although intrusion of both S- and I-type granites occurred in Late Devonian and Early Carboniferous times [*Williams*, 1989]. There has also been widespread emplacement of dolerite sheets in the Jurassic [*Elliot et al.*, 1991], which coincides with a period of extension that preceded the breakup of Gondwana.

[56] The implications of easterly dipping subduction during the Tyennan Orogeny in western Tasmania are significant. The Delamerian Orogeny, which represents the first phase of Phanerozoic accretion in eastern mainland Australia (Figure 1) is believed to have involved an eastward dipping subduction zone, and recent dating evidence points to rocks in western Tasmania and the Delamerian Orogen being similar in age [*Direen and Crawford*, 2003]. Given these constraints, and the likely presence of easterly dipping remnants of a past subduction zone in our tomographic model, the body of evidence for the Tyennan Orogeny in Tasmania representing the southern extension of the mainland Delamerian Orogeny is strong. The fact that the Moyston Fault (Figure 1), which marks the eastern edge of the Delamerian Orogen, trends to the west of Tasmania is not necessarily an argument against the joining of these two regions; *Betts et al.* [2002] provide evidence from plate reconstructions that Tasmania moved east relative to mainland Australia as a result of left lateral displacement along an east-west trending fault in Bass Strait during the first stages of rifting between Australia and Antarctica.

[57] The zone of relatively low velocity observed in Figure 15 is consistent with the idea that the central core of the Western Tasmania Terrane comprises siliciclastic Proterozoic continental material. *Cayley et al.* [2002] suggest that this Proterozoic crust extends northward beneath the cover of the Melbourne Zone (Figure 1). *Reed* [2001] proposes that the transition between Eastern and Western terranes extends northward to become the Governer fault, which separates the Tabberabbera and Melbourne zones. This implies that the Tabberabbera zone is underlain by crust of oceanic origin. While these models are yet to be fully tested, they, together with the results of our study, point to a clear link between the geology of Tasmania and mainland eastern Australia. Consequently, the tectonic evolution of Tasmania should not be considered separate to the formation of the Tasmanides.

8. Conclusions

[58] In this study, teleseismic tomography has been used to investigate the seismic structure of the crust and upper mantle beneath northern Tasmania. Relative arrival time residuals from distant events are picked using a robust adaptive stacking procedure. A new tomographic scheme based on the fast marching method and a subspace inversion method is used to map arrival time residuals from 101 earthquakes recorded by an array of 72 stations as 3-D perturbations in wave speed. Results indicate that the new scheme is both efficient and robust, making it well suited to large tomographic problems and the imaging of complex subsurface structures. A series of resolution tests show that the tomographic model of Tasmania is generally well constrained by the data set beneath the horizontal bounds of the array, although features with a scale length of approximately 20 km can only be recovered to depths of 80 km, and are subject to significant smearing by paths from the north. Features with a scale length of around 50 km can be recovered over a much larger region; for example, to nearly 180 km depth beneath the center of the array.

[59] The tomographic solution model exhibits the presence of coherent structure that can be related to the tectonic evolution of Tasmania and eastern mainland Australia. In particular, it is found that the sharp transition from relatively slow to relatively fast crustal velocities occurs to the east of the Tamar river, and is associated with a change from siliciclastic Proterozoic crust of continental origin to mafic crust of oceanic origin. Significantly, there is no evidence for the presence of a crustal scale suture zone beneath the so-called Tamar Fracture System, as has frequently been claimed. This suggests that the TFS is a thin skinned feature and that eastern and western Tasmania were joined well before the formation of the TFS in the mid-Devonian. Another important feature of the solution model is the presence of easterly dipping high-velocity structures in the lithosphere beneath western Tasmania. These may indicate the presence of an easterly dipping fossil subduction zone that is likely to have been active during the Middle to

Late Cambrian Tyennan Orogeny. If so, then this is further evidence that the Tyennan Orogeny in Tasmania represents the southern extension of the mainland Delamerian Orogeny, and hence that the tectonic evolution of Tasmania and mainland eastern Australia has been linked since the Cambrian.

[60] **Acknowledgments.** The authors would like to thank Steve Sirotjuk, Armando Arcidiaco, Stewart Fishwick, Trevor Allen, Malcolm Sambridge, Alexei Gorbatov, Tony Percival, and Dave Gatehouse for assistance with the deployment and servicing of seismic recorders. Thanks also go to Mineral Resources Tasmania, in particular, to Tony Brown and Bob Richardson for extensive logistical support and advice. The authors also appreciate the logistical support provided by the University of Tasmania. The Joint University Seismic Facility and Australian National Seismic Imaging Resource are acknowledged for providing a significant proportion of the seismic instrumentation. Last but not least, thanks go to the many private landowners and organizations, including Forestry Tasmania, Australia Bulk Minerals, Tasmania Parks and Wildlife Services, Gunns Limited, and Rayonier Tasmania, for permission to install seismometers on their land. N. Rawlinson is supported by Australian Research Council Discovery Project DP0556282.

References

Achauer, U. (1994), New ideas on the Kenya rift based on the inversion of the combined dataset of the 1985 and 1989/90 seismic tomography experiments, *Tectonophysics*, *236*, 305–329.

Aki, K., A. Christoffersson, and E. S. Husebye (1977), Determination of the three-dimensional seismic structure of the lithosphere, *J. Geophys. Res.*, *82*, 277–296.

Benz, H. M., G. Zandt, and D. H. Oppenheimer (1992), Lithospheric structure of northern California from teleseismic images of the upper mantle, *J. Geophys. Res.*, *97*, 4791–4807.

Betts, P. G., D. Giles, G. S. Lister, and L. Frick (2002), Evolution of the Australian lithosphere, *Aust. J. Earth Sci.*, *49*, 661–695.

Cayley, R., D. H. Taylor, A. H. M. VandenBerg, and D. H. Moore (2002), Proterozoic–Early Palaeozoic rocks and the Tyennan Orogeny in central Victoria: The Selwyn Block and its tectonic implications, *Aust. J. Earth Sci.*, *49*, 225–254.

Chevrot, S. (2002), Optimal measurements of relative and absolute delay times by simulated annealing, *Geophys. J. Int.*, *151*, 164–171.

Corbett, K. D., M. R. Banks, and J. B. Jago (1972), Plate tectonics and the Lower Palaeozoic of Tasmania, *Nature Phys. Sci.*, *240*, 9–11.

Crawford, A. J., and R. F. Berry (1992), Tectonic implications of Late Proterozoic-Early Palaeozoic igneous rock associations in western Tasmania, *Tectonophysics*, *214*, 37–56.

Crawford, A. J., S. Meffre, and P. A. Symonds (2003), 120 to 0 Ma tectonic evolution of the southwest Pacific and analogous geological evolution of the 600 to 220 Ma Tasman Fold Belt System, in *The Evolution and Dynamics of the Australian Plate*, edited by R. R. Hillis and R. D. Mller, *Spec. Publ. Geol. Soc. Aust.*, *22*, 383–404.

Debayle, E., and B. L. N. Kennett (2000), The Australian continental upper mantle: Structure and deformation inferred from surface waves, *J. Geophys. Res.*, *105*, 25,423–25,450.

Debayle, E., and B. L. N. Kennett (2003), Surface wave studies of the Australian region, in *The Evolution and Dynamics of the Australian Plate*, edited by R. R. Hillis and R. D. Mller, *Spec. Publ. Geol. Soc. Aust.*, *22*, 25–40.

Direen, N. G., and A. J. Crawford (2003), The Tasman Line: Where is it, what is it, and is it Australia's Rodinian breakup boundary?, *Aust. J. Earth Sci.*, *50*, 491–502.

Elliot, C. G., D. R. Gray, and N. B. Woodward (1991), Relating Tasmania to the Lachlan Fold Belt, *Geol. Soc. Aust. Abstr.*, *29*, 15.

Elliot, C. G., N. B. Woodward, and D. R. Gray (1993), Complex regional fault history of the Badger Head region, northern Tasmania, *Aust. J. Earth Sci.*, *40*, 155–168.

Fergusson, C. L. (2003), Ordovician-Silurian accretion tectonics of the Lachlan Fold Belt, southeastern Australia, *Aust. J. Earth Sci.*, *50*, 475–490.

Fishwick, S., B. L. N. Kennett, and A. M. Reading (2005), Contrasts in lithospheric structure within the Australian craton - insights from surface wave tomography, *Earth Planet. Sci. Lett.*, *231*, 163–176.

Foster, D. A., and D. R. Gray (2000), Evolution and structure of the Lachlan Fold Belt (Orogen) of eastern Australia, *Annu. Rev. Earth Planet. Sci.*, *28*, 47–80.

Frederiksen, A. W., M. G. Bostock, J. C. VanDecar, and J. F. Cassidy (1998), Seismic structure of the upper mantle beneath the northern Canadian Cordillera from teleseismic travel-time inversion, *Tectonophysics*, *294*, 43–55.

Graeber, F. M., G. A. Houseman, and S. A. Greenhalgh (2002), Regional teleseismic tomography of the western Lachlan Orogen and the Newer Volcanic Province, southeast Australia, *Geophys. J. Int.*, *149*, 249–266.

Gunn, P. J., T. E. Mackey, A. N. Yeates, R. G. Richardson, D. B. Seymour, M. P. McClenaghan, C. R. Calver, and M. J. Roach (1997), The basement elements of Tasmania, *Explor. Geophys.*, *28*, 225–231.

Humphreys, E. D., and R. W. Clayton (1990), Tomographic image of the southern California mantle, *J. Geophys. Res.*, *95*, 19,725–19,746.

Kennett, B. L. N., and E. R. Engdahl (1991), Traveltimes for global earthquake location and phase identification, *Geophys. J. Int.*, *105*, 429–465.

Kennett, B. L. N., M. S. Sambridge, and P. R. Williamson (1988), Subspace methods for large scale inverse problems involving multiple parameter classes, *Geophys. J.*, *94*, 237–247.

Kennett, B. L. N., E. R. Engdahl, and R. Buland (1995), Constraints on seismic velocities in the Earth from travel times, *Geophys. J. Int.*, *122*, 108–124.

Kennett, B. L. N., S. Fishwick, A. M. Reading, and N. Rawlinson (2004), Contrasts in mantle structure beneath Australia: Relation to Tasmania lines?, *Aust. J. Earth Sci.*, *51*, 563–569.

Kim, W., and C.-E. Baag (2002), Rapid and accurate two-point ray tracing based on a quadratic equation of takeoff angle in layered media with constant or linearly varying velocity function, *Bull. Seismol. Soc. Am.*, *92*, 2251–2263.

Leaman, D. E. (1989), The gravity field, in *Geology and Mineral Resources of Tasmania*, edited by C. F. Burrett and E. L. Martin, *Spec. Publ. Geol. Soc. Aust.*, *15*, 451–455.

Leaman, D. E. (1994), The Tamar Fracture System in Tasmania: Does it exist?, *Aust. J. Earth Sci.*, *41*, 73–74.

Lévêque, J. J., and F. Masson (1999), From ACH tomographic models to absolute velocity models, *Geophys. J. Int.*, *137*, 621–629.

Lévêque, J. J., L. Rivern, and G. Wittlinger (1993), On the use of the checker-board test to assess the resolution of tomographic inversions, *Geophys. J. Int.*, *115*, 313–318.

Lippitsch, R., E. Kissling, and J. Ansorge (2003), Upper mantle structure beneath the Alpine orogen from high-resolution teleseismic tomography, *J. Geophys. Res.*, *108*(B8), 2376, doi:10.1029/2002JB002016.

Oncescu, M. C., V. Burlacu, M. Anghel, and V. Smalbergher (1984), Three-dimensional *P*-wave velocity image under the Carpathian Arc, *Tectonophysics*, *106*, 305–319.

Popovici, A. M., and J. A. Sethian (2002), 3-D imaging using higher order fast marching traveltimes, *Geophysics*, *67*, 604–609.

Press, W. H., S. A. Tuekolsky, W. T. Vetterling, and B. P. Flannery (1992), *Numerical Recipes in FORTRAN*, Cambridge Univ. Press, New York.

Rawlinson, N., and B. L. N. Kennett (2004), Rapid estimation of relative and absolute delay times across a network by adaptive stacking, *Geophys. J. Int.*, *157*, 332–340.

Rawlinson, N., and M. Sambridge (2003), Seismic traveltime tomography of the crust and lithosphere, *Adv. Geophys.*, *46*, 81–198.

Rawlinson, N., and M. Sambridge (2004a), Wavefront evolution in strongly heterogeneous layered media using the Fast Marching Method, *Geophys. J. Int.*, *156*, 631–647.

Rawlinson, N., and M. Sambridge (2004b), Multiple reflection and transmission phases in complex layered media using a multistage fast marching method, *Geophysics*, *69*, 1338–1350.

Rawlinson, N., G. A. Houseman, and C. D. N. Collins (2001a), Inversion of seismic refraction and wide-angle reflection traveltimes for 3-D layered crustal structure, *Geophys. J. Int.*, *145*, 381–401.

Rawlinson, N., G. A. Houseman, C. D. N. Collins, and B. J. Drummond (2001b), New evidence of Tasmania's tectonic history from a novel seismic experiment, *Geophys. Res. Lett.*, *28*, 3337–3340.

Reading, A. M. (2005), Investigating the deep structure of terranes and terrane boundaries: Insights from earthquake seismic data, in *Terrane Processes at the Margins of Gondwana*, edited by A. P. M. Vaughan, P. T. Leat, and R. J. Pankhurst, *Geol. Soc. Spec. Publ.*, *246*, 293–303.

Reed, A. R. (2001), Pre-Tabberabberan deformation in eastern Tasmania: A southern extension of the Benambran Orogeny, *Aust. J. Earth Sci.*, *48*, 785–796.

Reed, A. R., C. Calver, and R. S. Bottrill (2002), Palaeozoic suturing of eastern and western Tasmania in the west Tamar region: Implications for the tectonic evolution of southeast Australia, *Aust. J. Earth Sci.*, *49*, 809–830.

Saltzer, R. L., and E. D. Humphreys (1997), Upper mantle *P* wave velocity structure of the eastern Snake River Plain and its relationship to geodynamic models of the region, *J. Geophys. Res.*, *102*, 11,829–11,841.

Sambridge, M. S. (1990), Non-linear arrival time inversion: Constraining velocity anomalies by seeking smooth models in 3-D, *Geophys. J. Int.*, *102*, 653–677.

Seber, D., M. Barazangi, B. A. Tadili, M. Ramdani, A. Ibenbrahim, and D. B. Sari (1996), Three-dimensional upper mantle structure beneath the intraplate Atlas and interplate Rif mountains of Morocco, *J. Geophys. Res.*, *101*, 3125–3138.

Sethian, J. A. (1996), A fast marching level set method for monotonically advancing fronts, *Proc. Natl. Acad. Sci. U.S.A.*, *93*, 1591–1595.

Sethian, J. A. (1999), *Level Set Methods and Fast Marching Methods*, Cambridge Univ. Press, New York.

Sethian, J. A. (2001), Evolution, implementation, and application of level set and fast marching methods for advancing fronts, *J. Comput. Phys.*, *169*, 503–555.

Sethian, J. A., and A. M. Popovici (1999), 3-D traveltime computation using the fast marching method, *Geophysics*, *64*, 516–523.

Shomali, Z. H., R. G. Roberts, and the TOR Working Group (2002), Nonlinear body wave teleseismic tomography along the TOR array, *Geophys. J. Int.*, *148*, 562–574.

Simons, F. J., R. D. van der Hilst, J.-P. Montagner, and A. Zielhuis (2002), Multimode Rayleigh wave inversion for heterogeneity and azimuthal anisotropy of the Australian upper mantle, *Geophys. J. Int.*, *151*, 738–754.

Spaggiari, C. V., D. R. Gray, D. A. Foster, and S. McKnight (2003), Evolution of the boundary between the western and central Lachlan Orogen: Implications for Tasmanide tectonics, *Aust. J. Earth Sci.*, *50*, 725–749.

Steck, L. K., C. H. Thurber, M. Fehler, W. J. Lutter, P. M. Roberts, W. S. Baldridge, D. G. Stafford, and R. Sessions (1998), Crust and upper mantle P wave velocity structure beneath Valles caldera, New Mexico: Results from the Jemez teleseismic tomography experiment, *J. Geophys. Res.*, *103*, 24,301–24,320.

Taylor, D. H., and R. A. Cayley (2000), Character and kinematics of faults within the turbidite-dominated Lachlan Orogen: Implications for tectonic evolution of eastern Australia: Discussion, *J. Struct. Geol.*, *22*, 523–528.

Turner, N. J., L. P. Black, and M. Kamperman (1998), Dating of Neoproterozoic and Cambrian orogenies in Tasmania, *Aust. J. Earth Sci.*, *45*, 789–806.

VanDecar, J. C. (1991), Upper-mantle structure of the Cascadia subduction zone from non-linear teleseismic travel-time inversion, Ph.D. thesis, Univ. of Wash., Seattle.

VanDecar, J. C., and R. S. Crosson (1990), Determination of teleseismic relative phase arrival times using multi-channel cross-correlation and least squares, *Bull. Seismol. Soc. Am.*, *80*, 150–169.

VandenBerg, A. H. M. (1999), Timing of orogenic events in the Lachlan Orogen, *Aust. J. Earth Sci.*, *46*, 691–701.

Waldhauser, F., R. Lippitsch, E. Kissling, and J. Ansorge (2002), High-resolution teleseismic tomography of upper-mantle structure using an a priori three-dimensional crustal model, *Geophys. J. Int.*, *150*, 403–414.

Wang, Y., and G. A. Houseman (1995), Tomographic inversion of reflection seismic amplitude data for velocity variation, *Geophys. J. Int.*, *123*, 355–372.

Williams, E. (1989), Summary and synthesis, in *Geology and Mineral Resources of Tasmania*, edited by C. F. Burrett and E. L. Martin, *Spec. Publ. Geol. Soc. Aust.*, *15*, 468–499.

Williamson, P. R. (1990), Tomographic inversion in reflection seismology, *Geophys. J. Int.*, *100*, 255–274.

Willman, C. E., A. H. M. VandenBerg, and V. J. Morand (2002), Evolution of the southeastern Lachlan Fold Belt in Victoria, *Aust. J. Earth Sci.*, *49*, 271–289.

Zelt, C. A., and P. J. Barton (1998), Three-dimensional seismic refraction tomography: A comparison of two methods applied to data from the Faeroe Basin, *J. Geophys. Res.*, *103*, 7187–7210.

Zielhuis, A., and R. D. van der Hilst (1996), Upper-mantle shear velocity beneath eastern Australia from inversion of waveforms from SKIPPY portable arrays, *Geophys. J. Int.*, *127*, 1–16.

B. L. N. Kennett, N. Rawlinson, and A. M. Reading, Research School of Earth Sciences, Australian National University, Canberra ACT 0200, Australia. (nick@rses.anu.edu.au)